A Wall-Modeled LES Perspective for the High Lift Common Research Model Using LAVA

Aditya S. Ghate*, Gaetan K.W. Kenway†,
Gerrit-Daniel Stich‡, Daniel Maldonado§ and Cetin C. Kiris¶
NASA Ames Research Center, Moffett Field, CA 94035

A new immersed boundary Wall-Modelled Large Eddy Simulation (WMLES) formulation is developed to study high-lift aerodynamics on the NASA High-Lift Common Research Model (HL-CRM). A sequence of Cartesian Octree grids with sizes ranging from 100 Million through 2.02 Billion grid points is utilized to systematically assess grid-sensitivity and convergence for the in-tunnel (QinetiQ) configuration of the model, and remarkable agreement between the immersed boundary and the curvilinear body-aligned WMLES formulations is reported on grids with comparable resolutions. In the free-air configuration of the model, consistent predictions between the Curvilinear Overset and the Cartesian Octree formulations are reported for angles of attack up to $C_{L,\mathbf{max}}$ at $\alpha = 19.57°$. However, some differences in the onset of stall are seen between the two methods for $\alpha > 20°$: while the curvilinear WMLES experiences wing-root separation with increasing angle of attack (Topology A), the Cartesian Octree formulation shows a different flow topology characterized by boundary layer weakness on the main element, emanating from the pylon-wing attachment (Topology B). In order to obtain further insight into the two-distinct topologies, carefully designed numerical experiments to isolate effects of the model standoff and the tunnel wall-boundary layers are conducted using the immersed boundary WMLES formulation. The increased incidence angle-of-attack on the inboard portion of the wing due to the standoff is shown to be sufficient for triggering a switch from Topology B to Topology A in Cartesian WMLES. The role of the floor boundary layer is further examined in detail by identification of additional corner-flow vorticity generated by the viscous juncture flow interactions between the floor boundary layer and the standoff leading to formation of a strong coherent and persistent vortex on the belly-side of the fuselage. The intensity of this vortex is shown to increase with the thickness of the floor boundary layer. A further increase in the incidence angle of attack near the leading-edge strake caused by the presence of this belly-side vortex is quantified for two-distinct floor boundary layers. Both of the floor boundary layers considered result in the onset of large scale wing-root separation at $\alpha = 21.47°$ in non-confined (free-air) configurations.

I. Introduction

Multiple recent and independently conducted studies[1–4] have now established the scope and potential of scale-resolving simulations at mitigating the various shortcomings of legacy steady-state Reynolds averaged Navier-Stokes (RANS) formulations for $C_{L,\max}$. Three prior high-lift prediction workshops (HLPW) conducted over the past decade detail some of these shortcomings[5–7]. In particular RANS simulations fail to accurately predict the flow-physics at $C_{L,\max}$ and the subsequent onset of stall at higher angles of attack. Furthermore, a few of the workshop submissions that do predict correct $C_{L,\max}$ values typically do so due to error cancellation[3, 8], and hence show large errors in pitching moment coefficients suggesting erroneous lift distributions. While the CFD Vision 2030 report[9] makes a case for research on scale-resolving simulations as a means to achieve the quantitative accuracy requirements formulated by the aerodynamics community[10], it also identifies automated and large-scale parallel grid generation as a key pacing item towards use of Computational Fluid Dynamics (CFD) as a tool for Certification and Qualification by Analysis (CQbA). While the research presented in this paper is largely a continuation of the recent work published in Kiris et al. (2022)[3], this second aspect pertaining to grid generation is an added focus of the present work.

*Science and Technology Corporation, AIAA Member, aditya.s.ghate@nasa.gov
†Science and Technology Corporation, AIAA Member, gaetan.k.kenway@nasa.gov
‡Science and Technology Corporation, AIAA Member, gerrit-daniel.stich@nasa.gov
§Computational Aerosciences Branch, AIAA Member, daniel.maldonado@nasa.gov
¶Computational Aerosciences Branch, AIAA Senior Member, cetin.c.kiris@nasa.gov

Consistent with the 4th High Lift Prediction Workshop (HLPW-4), the benchmark experiment used to compare the WMLES results is that of Evans *et al.* (2020)[11] studying the NASA 10% half-span model (see Figure 1) in the QinetiQ 5-meter wind tunnel (5mWT) located in Farnborough, UK. Beyond the geometry definitions provided, the entire problem is characterized by a mean-aerodynamic chord based Reynolds number of 5.5×10^6 and a free-stream (and test section reference) Mach number of 0.2. Case 2 of the HLPW-4 consisted of sub cases Case 2a and 2b which were the free air and wind tunnel configurations, respectively. The corrected and uncorrected aerodynamic loads, oil flow images, as well as pressure coefficients at various spanwise stations that were distributed via the HLPW4 webpage[12] are utilized throughout.

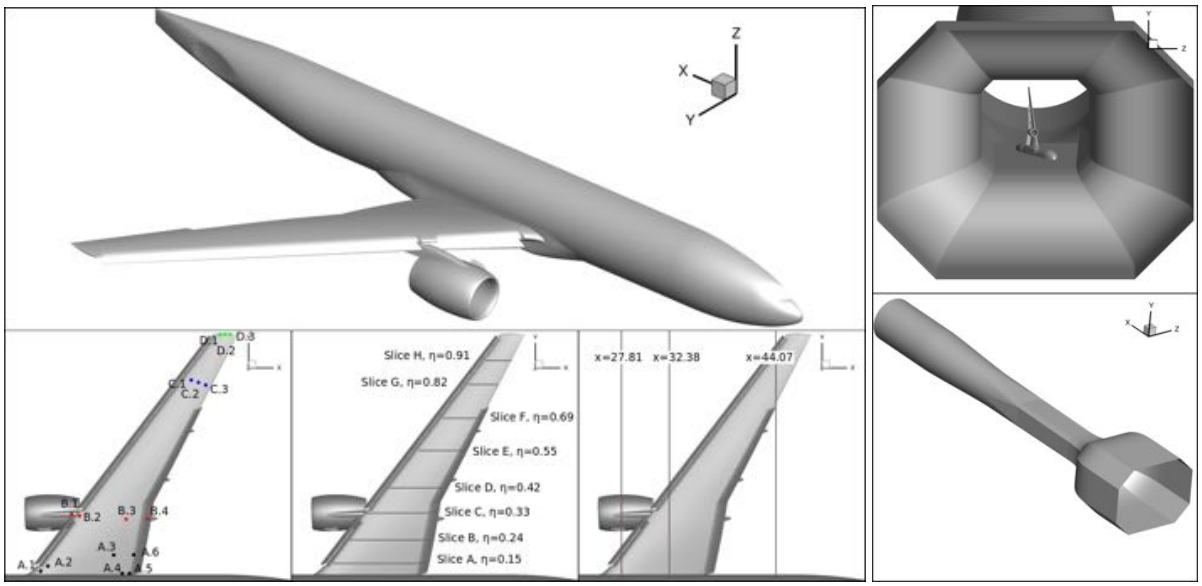

(a) Free Air (Case 2a) (b) Wind Tunnel (Case 2b)

Fig. 1 A schematic of the NASA 10%-scale semispan High Lift Common Research Model (CRM-HL) test article studied in this paper: (a) free air configuration (case 2a) and (b) wind tunnel configuration (case 2b). The lower three figures in (a) define locations on the CRM-HL (for both case 2a and case 2b) where particular flow quantities were recorded and used for comparison and validation , namely: (left) probes recorded unsteady pressure (c_P) at sixteen locations on the surface of suction side of the wing, (center) time-averaged pressure (c_P) was computed at eight different stations along the surfaces of the suction and pressure sides of the wing, (right) time-averaged vorticity was calculated along three slices going through the domain. Figure generated by Oliver Browne (NASA Ames Research Center).

We note that while an effort was made to make the present work a stand-alone contribution, the reader is encouraged to review the findings presented in Kiris et al. (2022)[3] prior to reading this paper. Some of the discussion that follows can be better appreciated if the reader is familiar with unified comparative summary of WMLES, Hybrid RANS/LES (HRLES) and RANS formulations that were the focus of the previous work. This paper is specifically targeted towards evaluation of a newly developed capability within the LAVA computational framework[13–18] that utilizes a Cartesian Octree grid topology with a new immersed boundary wall-modelled LES formulation developed by the authors. Beyond demonstrating the predictive capabilities of the new formulation for $C_{L,\max}$ applications, the work presented herein also sheds some light on phenomenological aspects of wall-interaction to allow for differentiation of in-tunnel simulations from free-air idealizations.

The paper is outlined as follows: we begin by introducing the Cartesian Octree grid paradigm along with a discussion on its benefits when compared with Structured Curvilinear Overset grid topologies in terms of grid-generation effort required by the two methods. A brief overview of the numerical discretization is also included in Section 2. The technical discussion of results starts in Section 3 with assessment of grid-sensitivities as well as comparisons between the curvilinear and the cartesian WMLES formulations for the in-tunnel configuration. Next some numerical experiments that systematically study the incremental effects of the model standoff and tunnel-floor boundary layer on the onset on

inboard stall are discussed in Section 4. Some remarks regarding computational cost of the new immersed boundary WMLES formulation compared with both steady-state RANS as well as curvilinear WMLES are provided in Section 5. A summary of the overall findings as well as potential future directions are discussed in Section 6 to wrap up the paper.

II. Numerical Formulation

A. Grid Systems

Wall-modelled Large Eddy Simulations (WMLES) were performed using two distinct mesh topologies: a) Structured Curvilinear Overset grids, and b) Cartesian Octree grids. Figure 2 shows a comparison between the two grid topologies on the HL-CRM model being studied.

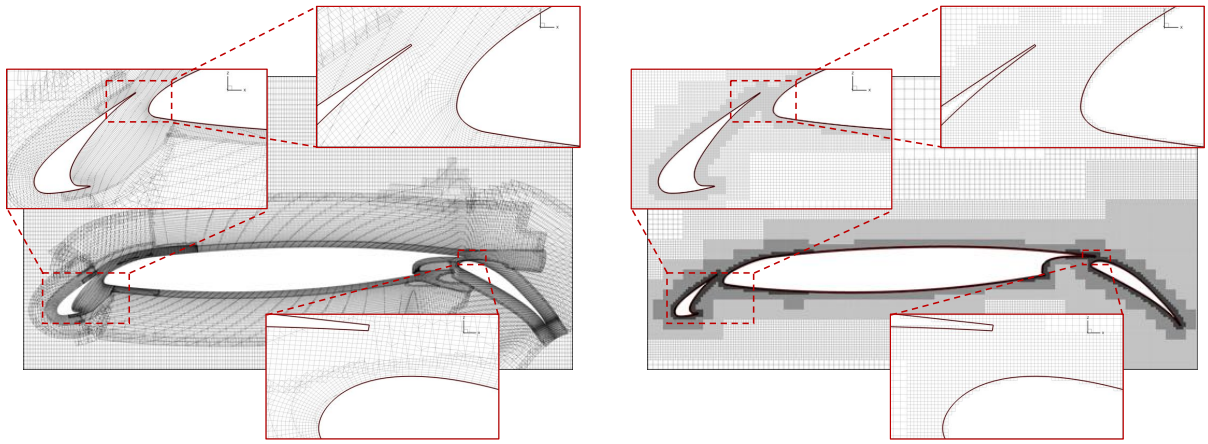

(a) Curvilinear Overset Topology

(b) Cartesian Octree Topology

Fig. 2 Representative grids for the two mesh topologies compared at a constant Y slice.

The primary advantage of the Cartesian Octree approach is the highly efficient and entirely automated grid generation procedure. This method relies only on a topologically regular surface triangulation and can be applied to arbitrarily complex geometries. Enforcement of unity aspect ratio has mixed consequence: a) it is excellent for resolving off-body vortical structures which lack a dominant direction of alignment, but b) requires larger number of grid points to match wall-normal spacing with a comparable curvilinear structured grid that utilizes non-unity aspect ratio near-wall cells. For the purpose of this study, local surface refinement near leading edges was avoided, and a more conservative refinement approach, where the entire suction side of the wing, slats, and flaps was refined to the nominal spacing, was utilized. This was to facilitate a consistent grid refinement study; however, future work will focus on utilizing localized refinement to reduce the total computational points. Table 1 provides a summary of the grid characteristics for the two different families of grids being considered in the present work.

In order to emphasize the grid-generation efficiency enabled by the Cartesian Octree approach, Figure 3 considers the single-node wall-time for grid generation for three topologies: a) cartesian octree, b) unstructured polyhedral, and c) structured overset curvilinear. Note that the wall-times represent the computational cost of generating the grid once the grid-system has been designed - this process involves determination of grid-spacings and refinement regions, and it took approximately 2 hours for the HL-CRM configuration presently being studied. The grid generation time can only be approximated for the curvilinear grids since this is a human-intensive task that requires on the order of months for an individual mesh generation expert on a configuration as complex as HL-CRM. The largest structured overset grid studied was with 1.1B grid points and required changes to the topology so that existing structured grid generation tools could be utilized. Furthermore, unlike the octree grids, all curvilinear overset grids required some minor changes to the geometry CAD model to faciliate grid generation. Some of these changes include a minor modifications to flap-gap and connection point between the slat-bracket and the slat cove. Thus, assuming comparable Navier-Stokes computational costs between curvilinear and Cartesian octree approaches (more on this in later sections), the utilization of Cartesian octree grids

Name	Solve Points	Off-wall spacing	Nominal Aspect Ratio	Comments
Grid W-A	275M	5mm (2.5mm near LE and flaps)	6-8	Baseline Grid
Grid W-B	360M	5mm (2.5mm near LE and flaps)	6-8	Grid W-A + (a)
Grid W-C	650M	5mm (2.5mm near LE and flaps)	2-3	Grid W-B + (b)
Grid W-D	1100M	2.5mm (5mm on wing pressure side)	4-6	Grid W-C + (c)
12mm, 100M	**100M**	**12mm (Isotropic)**	**1**	**Cartesian Octree Grid**
6mm, 450M	**450M**	**6mm (Isotropic)**	**1**	**Cartesian Octree Grid**
4mm, 1100M	**1100M**	**4mm (Isotropic)**	**1**	**Cartesian Octree Grid**
3mm, 2020M	**2020M**	**3mm (Isotropic)**	**1**	**Cartesian Octree Grid**

Table 1 Description of the grids utilized in this paper. The Cartesian Octree grids shown using bold-font are the focus of current work; results on the curvilinear grids are presented in [3]. (a) off-body refinement around the second overset layer off the wall (see Figure 2) and refinement block around the chine vortex (see Figure 37); (b) surface mesh was refined in stream-wise and span-wise direction on wing suction side and fuselage; (c) additional factor 2 refinement of wall-normal spacing on wing suction side as well as parts of the fuselage mesh.

represents a several months worth of reduced turnover time for obtaining the solution. The primary challenge for using such Cartesian grids is the solution algorithm which involves an immersed boundary representation of the geometry.

We note that a representative structured curvilinear overset grid (W-C) is publicly accessible via the High-Lift Prediction Workshop (HLPW-4) website[12]. A representative Cartesian Octree grid will also be made available via the same resource in the near future.

B. Discretization

A detailed discussion of the discretization used for structured curvilinear overset grids is provided in Kiris et al. (2022)[3]. Here we will limit the discussion to the Cartesian Octree formulation.

The inviscid flux discretization utilized a primitive variable blending of left and right biased 3rd order linear interpolations at midpoints with central 4th order accurate interpolation.

$$Q^{L}_{i+1/2} = (1-\zeta)Q^{L,3rd}_{i+1/2} + \zeta Q^{C,4th}_{i+1/2} \tag{1}$$

$$Q^{R}_{i+1/2} = (1-\zeta)Q^{R,3rd}_{i+1/2} + \zeta Q^{C,4th}_{i+1/2} \tag{2}$$

where Q represents a primitive variable. Nominally the blending factor, ζ is set to 0, and as such the midpoint interpolation is exactly central and hence non-dissipative. For the HL-CRM geometry considered, the blending factor, ζ is computed locally via a Ducros-type sensor[19] which restricts the usage of upwinding scheme in dilatationally dominant regions of the domain. This upwind sensor provides robustness in regions of strong acceleration occurring at high Mach numbers (such as on the suction side of the outboard slats). Figures 4 and 5 illustrate the ability of localized upwinding to mitigate spurious oscillations on the outboard slats at high angles of attack.

Evaluation of the inviscid flux at midpoint (as opposed to nodes) results in reduced aliasing errors (since midpoint interpolation of primitive variable is a low-pass filter operation) and hence provides non-linear robustness. Areas where $\zeta \neq 0$ include coarse-fine interfaces and trapped nodes - nodes where a discrete solution to Navier-Stokes cannot be obtained due to a lack of a 4th order accurate interpolation stencil. For trapped nodes, the linear upwind biased interpolation is replaced with a 3rd order accurate WENO interpolation[20]. Note that this is consistent in spirit with Weighted Compact Non-linear Schemes (WCNS)[21, 22], although we emphasize that non-linear interpolations are only performed at trapped nodes. A 4th order accurate derivative-of-flux midpoint-and-node operator[23] is used to compute the divergence of inviscid flux.

While a detailed discussion of the new immersed boundary wall-modelled LES formulation is beyond the scope of the present work and will be addressed in a future manuscript, we note a few salient attributes pertinent for the present HL-CRM simulations. A ghost-cell method[24] is used to represent the inviscid effect of geometry. Convective flux discretization is fourth order-accurate everywhere - this is accomplished by avoiding any stencil changes near the

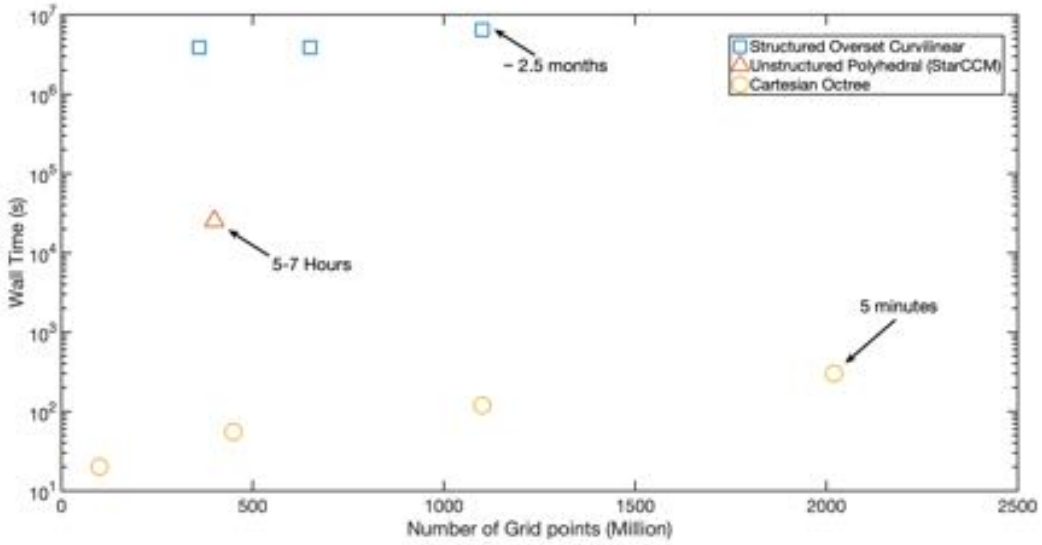

Fig. 3 Wall-times for generating WMLES grids for HL-CRM using three different mesh topologies. Curvilinear wall-times include manual labor hours of subject-matter meshing expert.

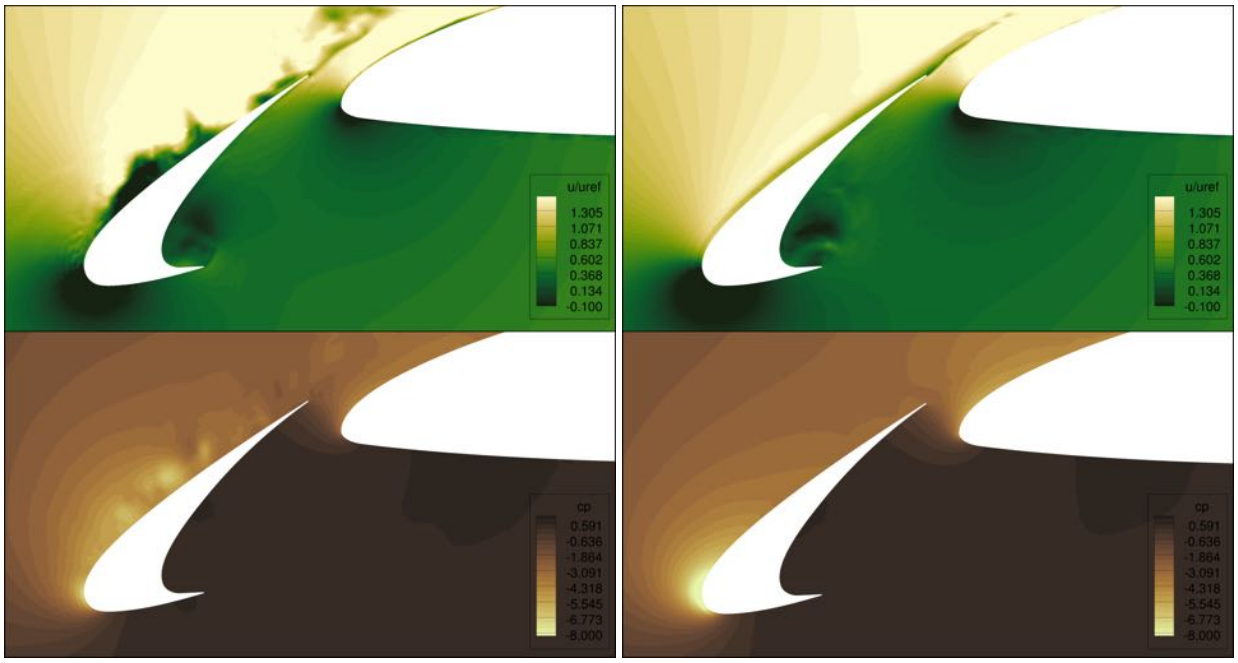

(a) 4th order central mid-point interpolation (not robust for LES)

(b) 3rd Order/4th order sensor-based blended interpolation (very robust for LES)

Fig. 4 Instantaneous x-directional velocity and coefficient of pressure at $y = 23m$ plane for $\alpha = 19.57°$ case showing the effect of numerical discretization on controlling non-physical spurious oscillations. Contours are shown for the curvilinear Grid W-B.

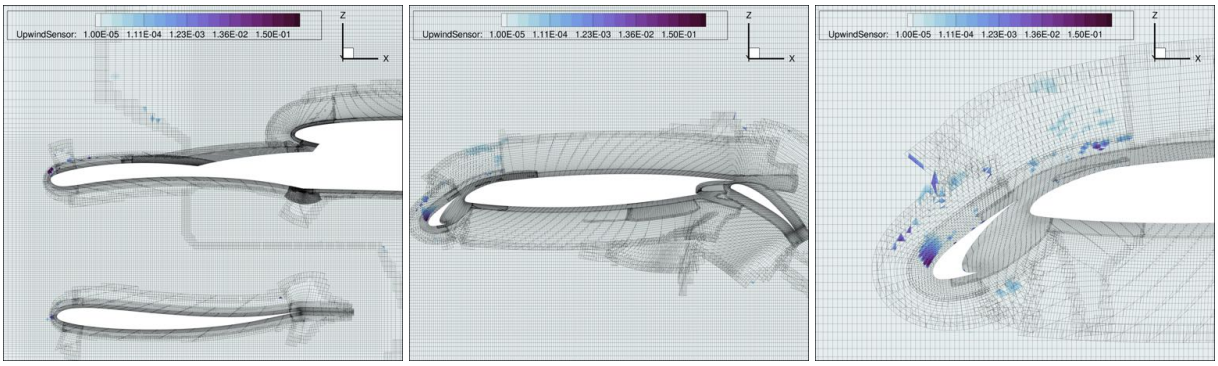

(a) $y = 10m$ (b) $y = 18m$ (c) $y = 23m$

Fig. 5 Instantaneous upwind sensor for $\alpha = 19.57°$ on the curvilinear grid W-B. Blue regions highlighted correspond to grid points where non-zero blending between 3rd order upwind biased interpolation and 4th order central interpolation is used. Note that the colormap uses an exponential axis corresponding to the ratio of 3rd order upwind biased interpolation. The upwind sensor used here is of the form, $\zeta = \left(\frac{\Omega^2}{\Omega^2+\Theta^2}\right)^n$ where Ω is the local enstrophy and Θ is the local dilatation computed at midpoints using staggered differential operators. Present work uses $n = 4$ in order to localize the use of upwind schemes further and to minimize any interactions with numerically transitioning leading edge boundary layers.

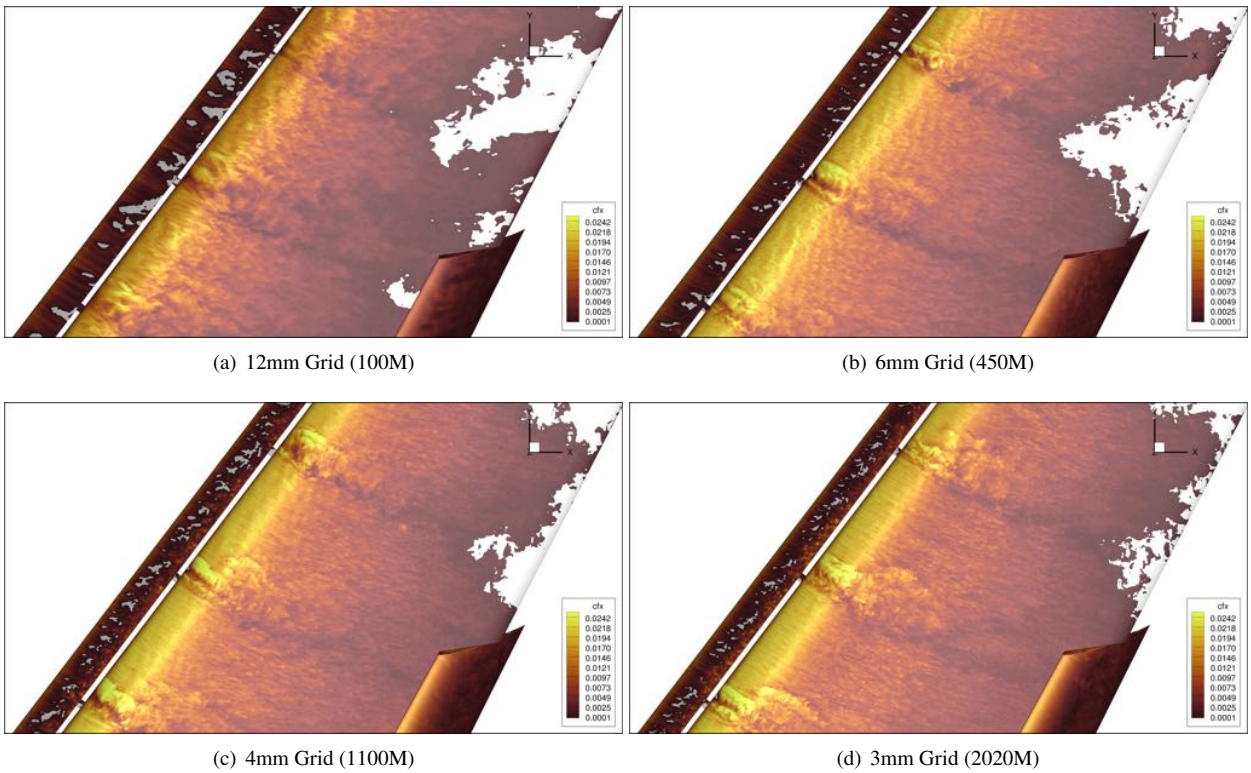

(a) 12mm Grid (100M) (b) 6mm Grid (450M)

(c) 4mm Grid (1100M) (d) 3mm Grid (2020M)

Fig. 6 Instantaneous surface skin-friction (c_{Fx}) on the suction side of the wing towards the outboard region at $\alpha = 19.97°$ (in tunnel). The white (clipped) regions correspond to $c_{Fx} < 0$.

geometry. All simulations are run with no upwinding (except for use of an upwind sensor as discussed previously).

1) **Complex geometry handling** : Fully consistent ghost cells are used regardless of geometry complexity (sharp corners, thin edges) by using appropriate computer science techniques (special data structures for ghost cells and algorithms for setting their geometry+stencil-aware values).
2) **Spurious dilatational and entropic content** : Special numerical treatment was designed to address spurious content generated by the ghost-cell method without utilizing either near-wall upwinding or spatial filtering since both approaches were deemed to affect any wall-bounded turbulence being resolved - especially involving coarse-representation of boundary layers.
3) **Wall-stress treatment**: Specific formulation for wall-stress boundary condition was developed. The formulation ensures that the full-wall stress is applied when boundary stress-tensors are rotated in the wall-aligned frame of reference and momentum conservation in this rotated frame is enforced at the walls.

Figure 6 shows instantaneous surface skin friction for the 4 Cartesian grid levels investigated. It highlights the lack-of Cartesian imprinting (stair-stepping) that is often observed in other immersed boundary formulations. The present formulation does not suffer from such errors even at the coarsest grid levels and the boundary layers transition to turbulence naturally due to growth of round-off errors.

The methodology has been validated using a sequence of increasingly complex wall-bounded flows including: a) zero-pressure gradient grid aligned and misaligned flat plates, b) NASA wall-mounted hump[25, 26], c) NACA 23012 airfoil with leading edge icing[27], and d) the LAGOON landing gear[28, 29].

Wall modeling is performed using an analytic log law with smooth blending between the viscous sublayer and log-layer (with wall-model exchange location set to 1Δ from the wall), and the constant coefficient Vreman model[30] is used for subgrid scale closure. The Total-Variation Diminishing (TVD) variant of RK-4[31] is used for time discretization.

III. Wind Tunnel Configuration

We begin the technical discussion of the results by first considering the in-tunnel simulations. The initialization procedure is discussed first followed by a systematic investigation of grid sensitivity along with comparisons with the curvilinear WMLES.

A. Initialization procedure

All immersed boundary WMLES studied, except for the 3mm (2.02B grid points) grid case, were initialized identically via the following three-step procedure:

1) **Steady-State solve**: Wall-modelled steady-state RANS simulation using a very coarse mesh (64mm minimum spacing) is performed to calibrate the back-pressure at each angle of attack. In the present work, curvilinear grids were utilized for this steady state solve followed by interpolation to the precursor Cartesian Octree grid. Assuming unavailability of a curvilinear steady-state solver, we anticipate a need to perform long-time integrated of the empty tunnel configuration followed by re-initialization with the model in the tunnel. This approach would require the use of a back-pressure controller due to large differences in the back-pressure needed to obtain the reference test section Mach number(see Ref. [32])) between simulations with and without the test-article. Proportional-Integral-Derivative (PID) controllers that modify the tunnel back-pressure have been shown to be successful at achieving target reference Mach numbers[33]. However, since the curvilinear steady-state WM-RANS data was already available from our previous studies[3], this step could be avoided.
2) **Precursor Simulation**: The interpolated solution on the 64mm precursor grid is time evolved over a period of at least 1000 CTUs (CTU = $tu_{\text{ref}}/c_{\text{MAC}}$). This allows the wake of the geometry to propagate downstream to the tunnel outlet via an LES-closure, and allows the tunnel boundary-layers to develop to the stationary state. Roughness treatment was used upstream of the test-section to trigger transition and artificially thicken the boundary layer. The reader is referred to Kiris et al. (2022)[3] for a thorough discussion of the level of agreement achieved by WMLES with the experimental rake measurements. Minor back-pressure changes are needed although the differences between the RANS-calibrated back-pressures and the asymptotic back-pressures for WMLES were less than $5 \times 10^{-4} \text{P}_{\text{ref}}$ where P_{ref} is the test-section reference pressure.
3) **Primary Simulation**: The precursor solution data is interpolated on the specific primary grid being utilized (example for the 4mm grid is shown in Figure 8 at $\alpha = 19.98°$). All angles (with the exception of 19.98° case) are simulated for at least 20CTU of the primary grid before statistical averaging is performed. The 19.8° case showed a strong pitch break that occurred at varying times depending on the primary grid being used. For

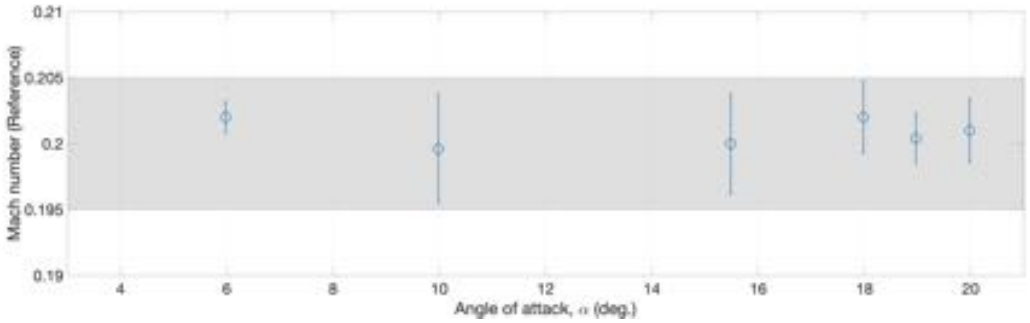

Fig. 7 Reference Mach numbers achieved in the test section (based on the QinetiQ-tunnel calibration procedure). The symbols and error bars represent the time-averaged value and 1 standard deviation through the duration of statistical averaging of aerodynamic loads. The grey shaded region represents the *acceptable values* - where the effective changes to the momentum flux (and Reynolds number) are insignificant. Note that the non-dimensional loading coefficients need to be re-scaled based on the time-averaged reference Mach numbers for each angle of attack.

example, the onset of pitch-break occurred on the 12mm grid after 120CTUs, while it occurred on the 4mm grid after approximately 25CTUs of interpolation from precursor grid. Simulations with $\alpha < 18.9°$ were statistically averaged for at least 30CTUs. The $\alpha = 18.9°$ and $\alpha = 19.9°$ were statistically averaged for over at least 75CTUs after the onset of pitch-break followed by stationarity. The 3mm grid simulations were initialized from the final simulated snapshot from the 4mm grid simulations. The initial 10CTUs were rejected from statistical averaging in order to exclude grid-related transience. Averaging intervals for 3mm simulations were identical to the averaging intervals for other simulations.

Since the back-pressure for the primary grid simulations is not changed throughout the simulation, some drift/change in the reference Mach number can be expected. Figure 7 shows the average reference mach number along with its standard deviation through the statistical sampling interval for each angle of attack investigated. We remark that the Mach numbers achieved for each simulated angle are within recommended tolerance[32]. Furthermore, note that the tunnel wall-grids (64mm in the test-section) are identical between the precursor and primary simulations with any mesh differences restricted to the test-article. Figure 8 shows a comparison of the instantaneous Mach number between the precursor and the 4mm primary simulation grid.

B. Grid refinement and comparisons with Curvilinear WMLES

The integrated lift, drag and pitching moment coefficients are shown in Figure 9. While some sensitivity going from the 12mm grid to the 3mm grid is observed for $\alpha < 15°$ due to small changes to the flap separation, it is most notably present in pitching moment values for $\alpha > 15°$. Several interesting observations follow:

1) At $\alpha = 5.9°$, the grid convergence trend suggests that the coarser grids over-predict aft-loading (downstream of the pitching axis) - since the drop in lift results in a tendency for a more nose-up pitching moment. Note that while we do not expect such coarse simulation to accurately capture the shallow smooth-body separation - low-Reynolds number character of the flap boundary layer is likely to be a problem - it is nonetheless promising to see that the Cartesian WMLES predict the low-α loading with high accuracy. This is in stark contrast to RANS data* which show a large tendency for a nose-up pitching moment which is due to excess flap-separation predicted by the steady-state solves. Additional grid-studies are needed to fully understand the WMLES-predicted flap separation, although this is currently not feasible due to computational resource restrictions. Curvilinear WMLES and the 4mm and 3mm grid Cartesian WMLES appear to be in excellent agreement amongst themselves and with the experimental observations. Similar observations apply to the $\alpha = 9.9°$ case.
2) To understand the sensitivities in integral loads for $\alpha > 15°$, we consider the surface distribution of lift and pitching-moment in terms of the load integrands - that are integrated via trapezoidal quadrature to obtain the integral C_L and $C_{M,y}$ for the full test article. These are shown in Figures 10 through 13. For $\alpha = 15.5°$ and $\alpha = 17.9°$ cases, it is very evident that the 12mm grid is suboptimal for predicting suction on the outboard wing.

*see [3] for additional details regarding the RANS data

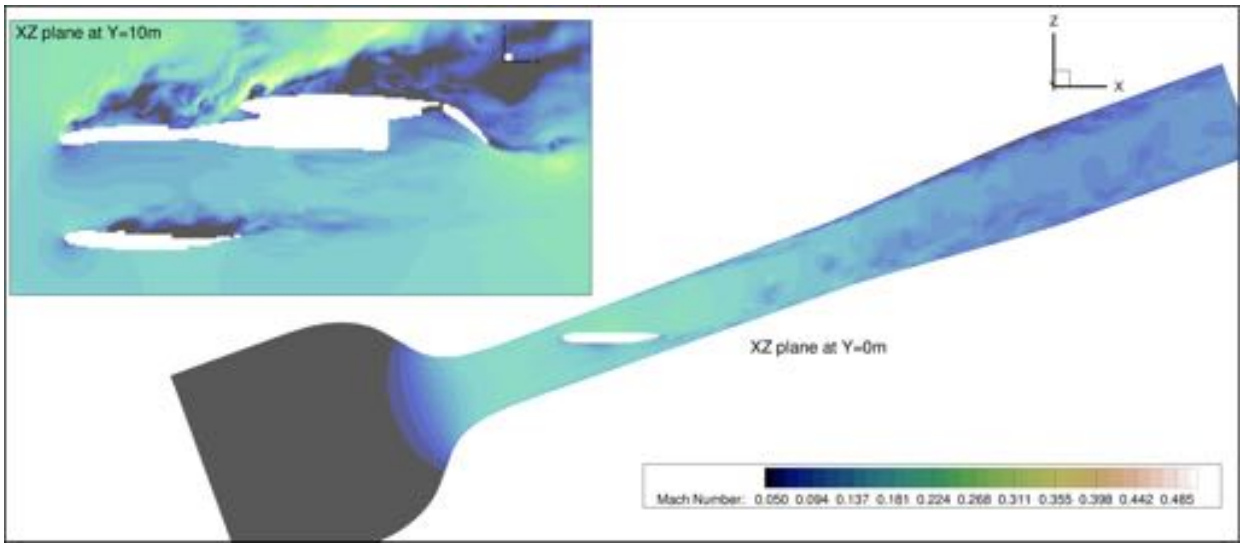

(a) **Precursor Simulation (64mm resolution)**: To develop the tunnel boundary layer and to propagate model wake to the tunnel outflow. Simulated for >1000 CTUs.

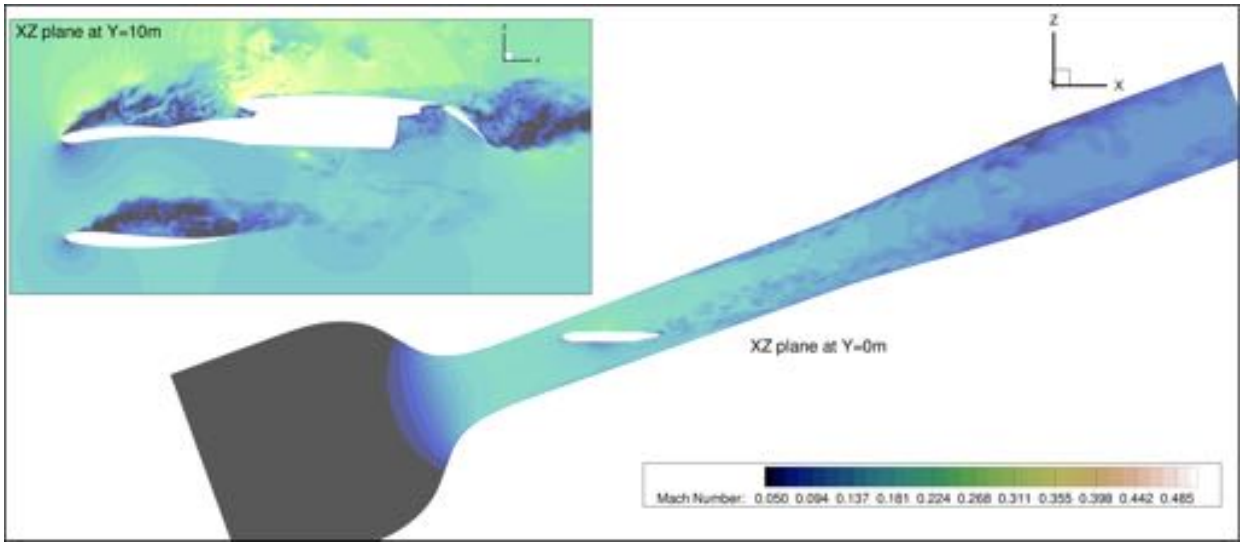

(b) **Primary Simulation (4mm resolution)**: For computing aerodynamic loading and flow-topology analysis, solution interpolation from precursor grid and statistical averaging is performed after flushing out the first 20 CTUs.

Fig. 8 Instantaneous Mach number visualized on XZ planes for in-tunnel WMLES at $\alpha = 19.98°$.

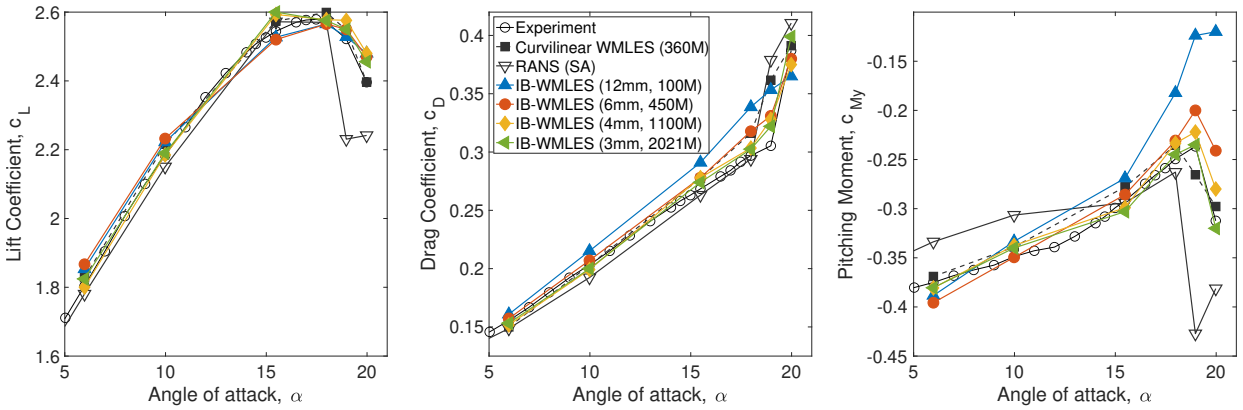

Fig. 9 Integrated forces and moments for in-tunnel simulations

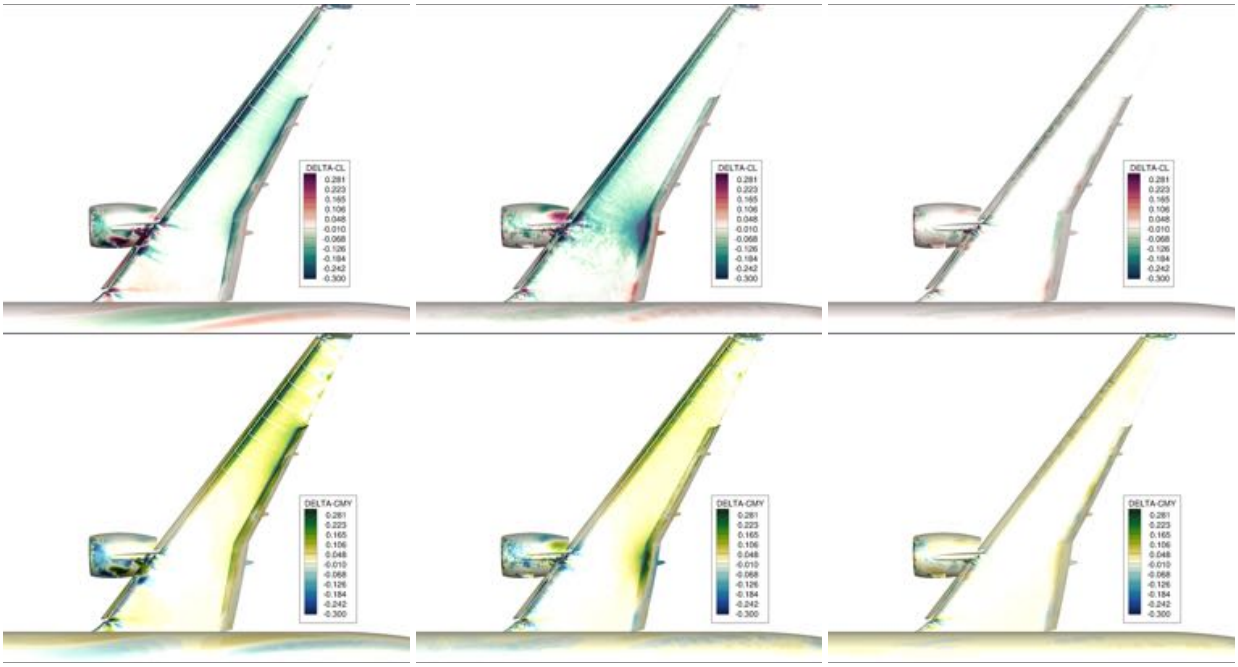

(a) 12mm Grid (100M) (b) 6mm Grid (450M) (c) 4mm Grid (1100M)

Fig. 10 Difference in the lift and pitching moment coefficient integrands with respect to the reference 3mm (2021M) grid at $\alpha = 15.48°$. In the CL integrand considered in the top level, green-regions indicate lower suction compared to the reference grid, while red regions indicate higher suction. Similarly, in the CMY integrand considered in the bottom level, green regions indicate a lower nose-down moment being generated compared to the reference grid, while blue regions indicate that a higher nose-down moment is generated.

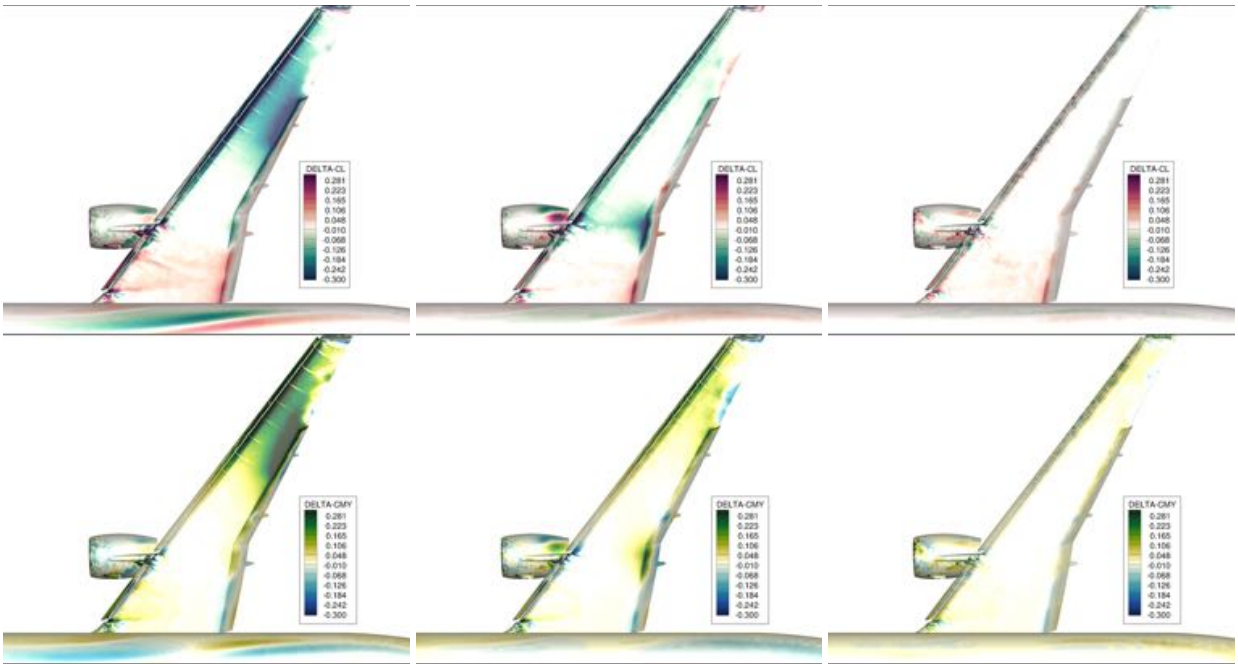

(a) 12mm Grid (100M) (b) 6mm Grid (450M) (c) 4mm Grid (1100M)

Fig. 11 Caption same as Figure 10 but at $\alpha = 17.98°$.

This is likely do to lack-of-resolution available in the grids to capture the inviscid acceleration caused by the high-curvature on the outboard slats and main-element leading edge. The 6mm grid performs significantly better, although some differences near the flap-gap are glaring. Note that the difference between ΔC_L for the 12mm grid and 6mm grid indicates that the convergence is non-monotonic even if the integral values suggest this. In other words, via refinement regions of the geometry with improved predictions may not necessarily be the same. Furthermore, it is very evident that the fuselage vortex (caused by the roll-up of the boundary layer at the azimuth) is inadequately captured by the 12mm grid. The symmetric nature of both ΔC_L and $\Delta C_{M,y}$ leads to little difference in the integral load; however, this visualization (see Figure 10a - 12a) clearly shows that time-average fuselage vortex for the 12mm grid is erroneous.

3) The effect of grid refinement for the Cartesian WMLES at $\alpha = 15°$ leads to a tendency for a larger-nose down moment compared to the experiment. This is unlike the curvilinear WMLES which predicts an excess nose-up pitching moment for all $\alpha > 15°$. Interestingly, this excess nose-down moment seen in the 4mm and 3mm Cartesian WMLES is correlated with an excess C_L at $\alpha = 15.5°$. Analysis in terms of the integrands (see Figure 10) suggests that this increase in suction going from 6mm to the 4mm grid comes from the outboard flaps. This effect is also observed at $\alpha = 17.9°$. The pressure coefficients at three stations on the outboard flap are shown in Figure 18. Remarkably - the 4mm and 3mm Cartesian grids produce flap suction more accurately than the curvilinear grid WMLES! This results in larger-CL and a more nose-down pitching moment for the Cartesian WMLES compared to the Curvilinear WMLES - hence the Cartesian WMLES is more in line with the experimental observation.
4) For $\alpha < 18°$ the 4mm grid produced aerodynamic loading essentially equivalent to the 3mm grid (see Figures 10c and 11c). This also translates to identical surface flow topology between the two grids as shown in Figures 14 - 15. In these time-averaged surface flow visualizations, it is also abundantly clear that the outboard flow is inaccurately predicted by the 12mm grid - which unlike 6mm and finer grids, fails to develop the wedge-shaped separation patterns at $\alpha = 15.5°$ and develops an excessively separated outboard flow at $\alpha > 17.9°$. The outboard flow topology seen in the 6mm, 4mm and 3mm grids is essentially identical and largely consistent with the topology seen in the experiments via oil flow visualizations[34].
5) A stark shift in convergence pattern appears for $\alpha > 18.9°$ - this is associated with the onset of inboard stall. The changes to ΔC_L and $\Delta C_{M,y}$ now are dominated by the flow inboard of the Yehudi break (see Figures 12 and 13).

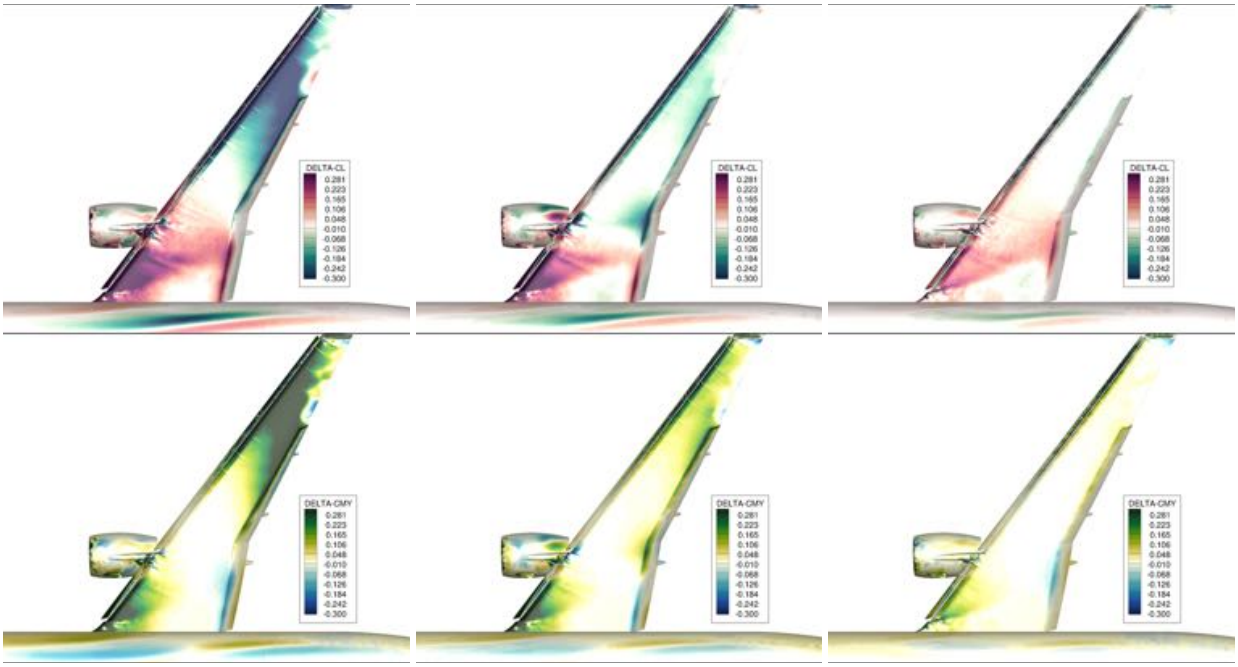

(a) 12mm Grid (100M) (b) 6mm Grid (450M) (c) 4mm Grid (1100M)

Fig. 12 Caption same as Figure 10 but at $\alpha = 18.97°$.

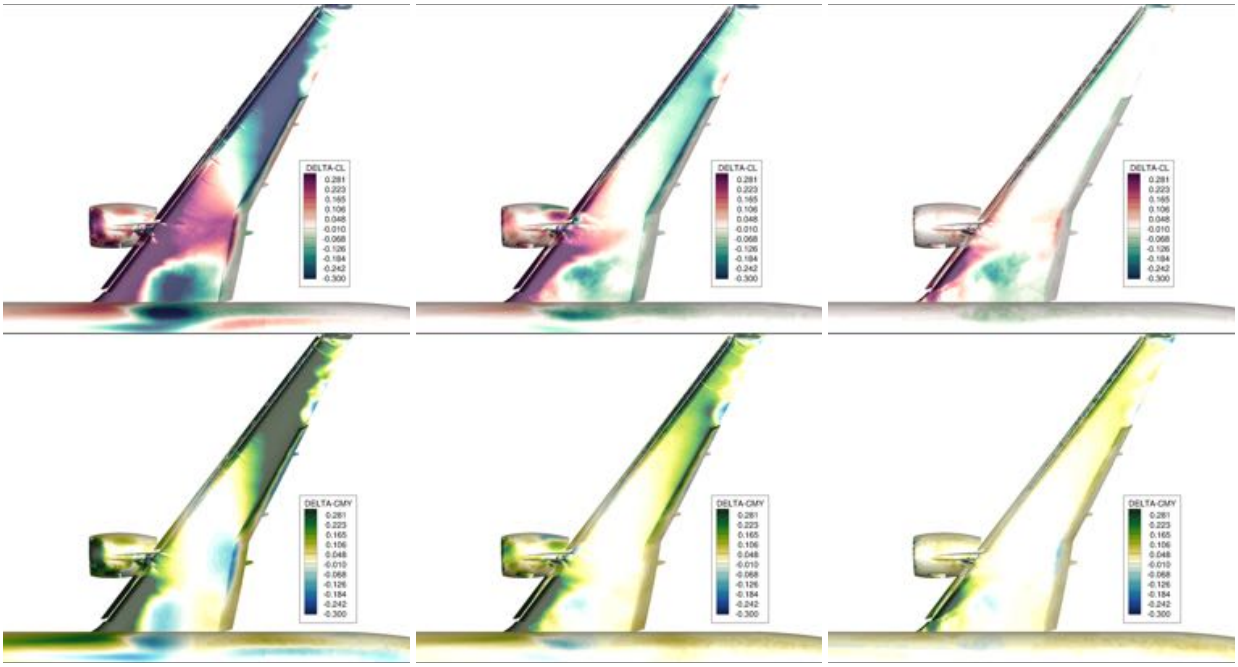

(a) 12mm Grid (100M) (b) 6mm Grid (450M) (c) 4mm Grid (1100M)

Fig. 13 Caption same as Figure 10 but at $\alpha = 19.98°$.

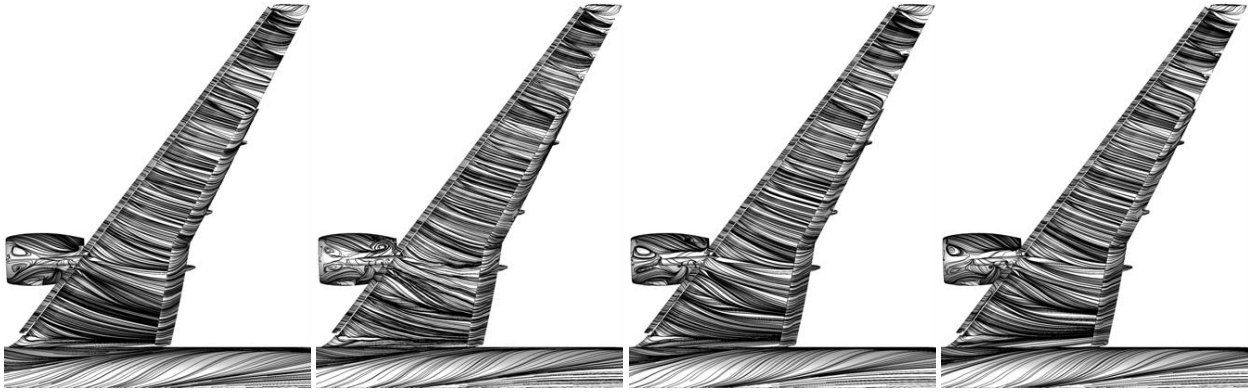

(a) 12mm Grid (100M) (b) 6mm Grid (450M) (c) 4mm Grid (1100M) (d) 3mm Grid (2021M)

Fig. 14 Surface skin-friction streamlines for the 4 grids levels at $\alpha = 15.48°$.

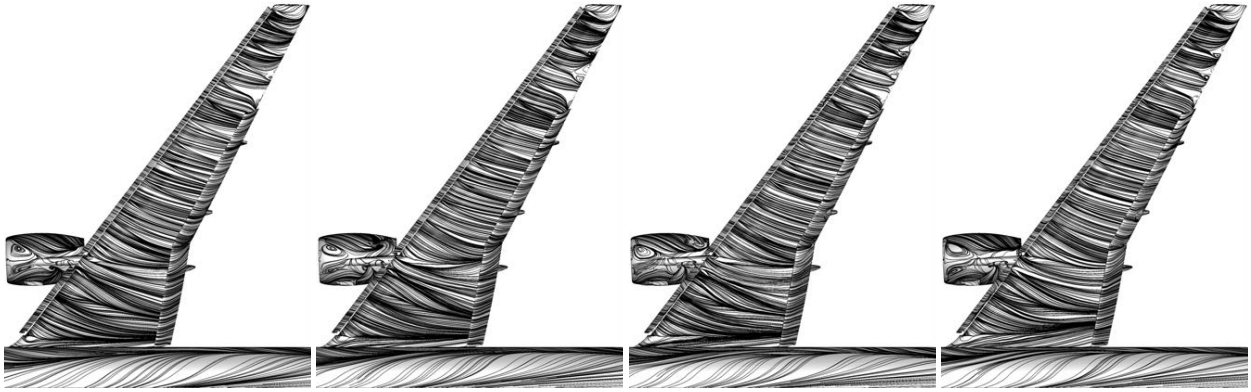

(a) 12mm Grid (100M) (b) 6mm Grid (450M) (c) 4mm Grid (1100M) (d) 3mm Grid (2021M)

Fig. 15 Surface skin-friction streamlines for the 4 grids levels at $\alpha = 17.98°$.

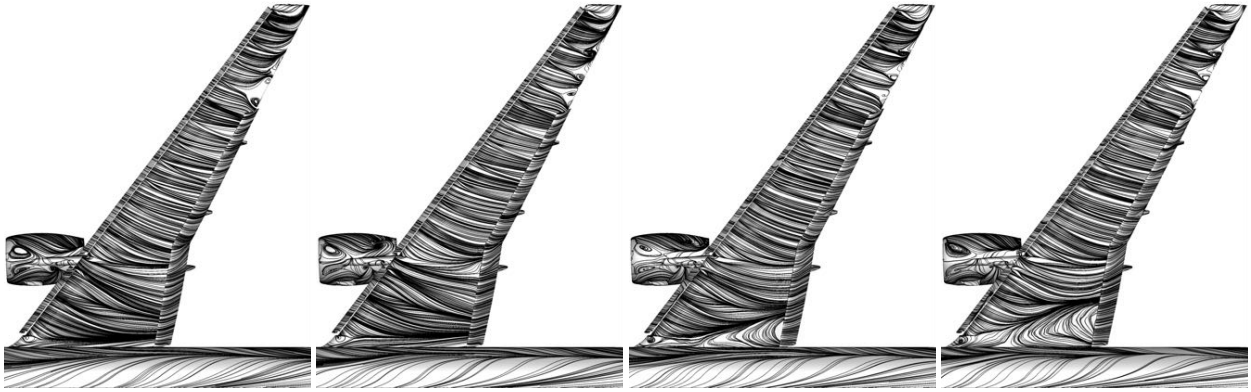

(a) 12mm Grid (100M) (b) 6mm Grid (450M) (c) 4mm Grid (1100M) (d) 3mm Grid (2021M)

Fig. 16 Surface skin-friction streamlines for the 4 grids levels at $\alpha = 18.97°$.

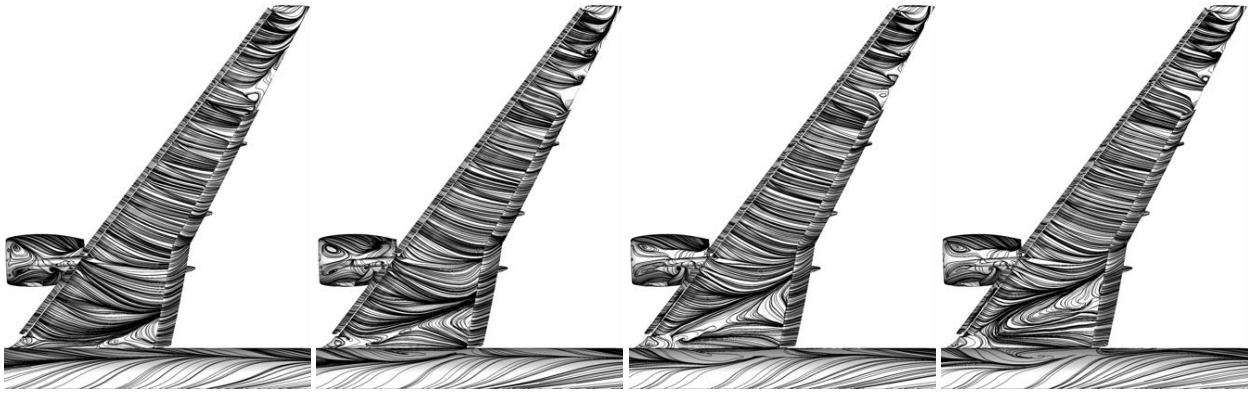

(a) 12mm Grid (100M) (b) 6mm Grid (450M) (c) 4mm Grid (1100M) (d) 3mm Grid (2021M)

Fig. 17 Surface skin-friction streamlines for the 4 grids levels at $\alpha = 19.98°$.

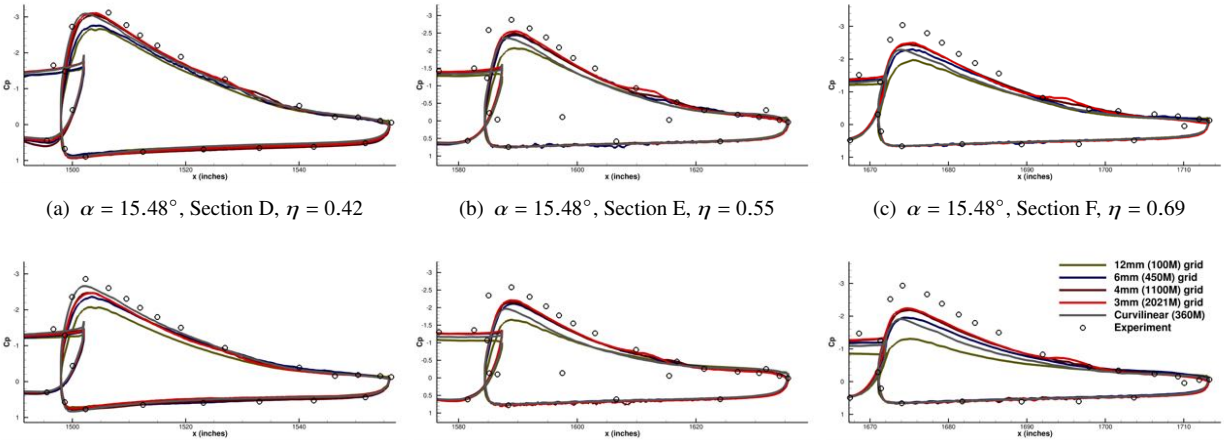

(a) $\alpha = 15.48°$, Section D, $\eta = 0.42$ (b) $\alpha = 15.48°$, Section E, $\eta = 0.55$ (c) $\alpha = 15.48°$, Section F, $\eta = 0.69$

(d) $\alpha = 17.98°$, Section D, $\eta = 0.42$ (e) $\alpha = 17.98°$, Section E, $\eta = 0.55$ (f) $\alpha = 17.98°$, Section F, $\eta = 0.69$

Fig. 18 Coefficient of Pressure on the outboard flap near $C_{L,\mathbf{max}}$.

The streamlines shown in Figures 16 - 17 show a consistent trend towards an increase in wing-root separation with resolution. Non-trivial change is observed between 4mm and 3mm grids suggesting that further resolution studies should be conducted to assess further convergence. Futhermore, coarser grids also appear to overpredict suction downstream of the pylon mount (see Figure 12c) and outer midboard portions of the wing. The cause of this is unclear at this time - although the nacelle separation observed in all simulations for $\alpha > 15^\circ$ could potentially be the source of this overprediction. The $\alpha = 19.9^\circ$ shows a strong pitch break, with the strongest break observed in the 3mm grid. On the 3mm grid, while the pitching moment coefficient shows excellent agreement with the experimental data, the C_L predicted by all grids at $\alpha = 19.9^\circ$ is consistently larger than the experiment value by approximately 2%. The pressure coefficient comparisons at all 8 stations shown in Figure 19 offer some insight.

a. The excess suction appears to come entirely from the portion of the main-element directly downstream of the Nacelle/Pylon mount. This does not occur in the curvilinear grid solutions. One potential explanation is the excess nacelle-separation seen in the Cartesian grids; note that the free-air simulations using curvilinear WMLES show increasing nacelle-separation with grid refinement. Unfortunately a finer grid in-tunnel curvilinear WMLES was not performed, and so whether subsequent grid-refinement would increase suction in the curvilinear WMLES remains to be seen. Since the excess suction in cartesian simulations is distributed symmetrically about the pitching axis, the error does not show up in the integrated pitching moment coefficient which is in remarkable agreement with the experiment data.

b. The 3mm cartesian grid shows the best agreement for the inboard pressure coefficient (Sections A and B, in Figure 19) out of all WMLES (including curvilinear grid simulations) analysed. The suction peak near the leading edge followed by the flattened CP curve for the 3mm grid is more accurate in the 3mm grid Cartesian WMLES than the curvilinear WMLES.

c. While the 12mm grid predicts a suboptimal outboard suction at $\alpha > 17^\circ$, we note that it is still substantially more accurate than steady-state RANS which predicts massive spurious outboard separation that becomes increasingly inaccurate with grid refinement (see Kiris et al. (2022)[3]). This is in contrast with the WMLES studied here where an improvement in accuracy is observed with every level of refinement without exception.

6) Surface flow topology at the stalled state ($\alpha = 19.9^\circ$) is shown in Figure 20 via comparisons between the 3mm Cartesian WMLES, the curvilinear WMLES, steady state RANS and the oil flow photographs. We note the remarkable agreement between the curvilinear and Cartesian WMLES which predict a large region of wing root separation along with a large curled vortex on the fuselage in agreement with the oil flow. On the other hand, RANS predicts unphysically large inboard separation along with unphysically large outboard separation. Both curvilinear and Cartesian WMLES predict an outboard surface flow topology showing the wedge-shaped separation patterns. While the curvilinear WMLES shows slighly smaller outboard separation regions compared to the Cartesian, this is likely due to under-resolution in the curvilinear simulations. Grid refinement studies in free-air showed increasing separation regions with finer lever grids for curvilinear WMLES.

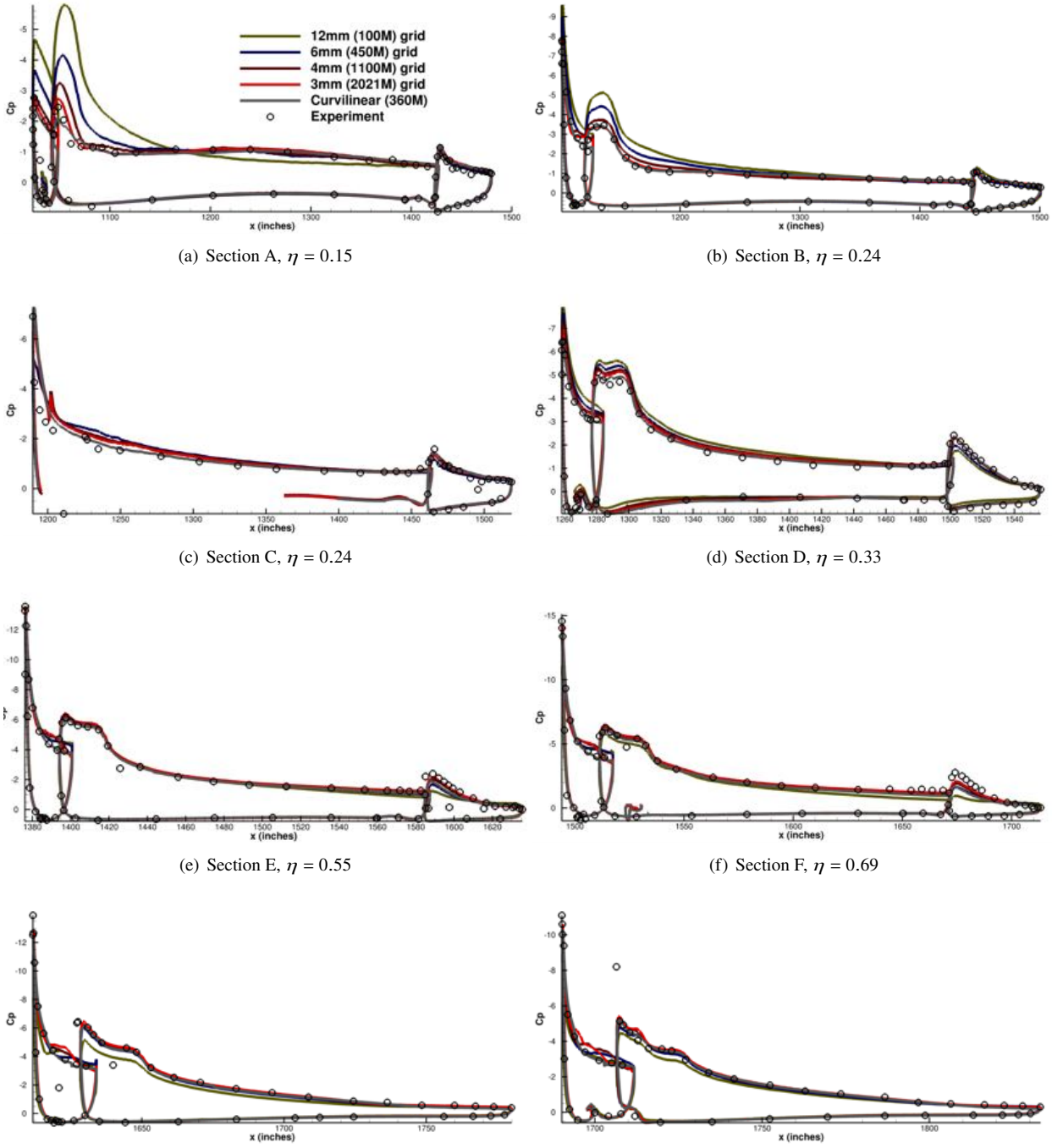

(a) Section A, $\eta = 0.15$

(b) Section B, $\eta = 0.24$

(c) Section C, $\eta = 0.24$

(d) Section D, $\eta = 0.33$

(e) Section E, $\eta = 0.55$

(f) Section F, $\eta = 0.69$

(g) Section G, $\eta = 0.82$

(h) Section H, $\eta = 0.91$

Fig. 19 Coefficient of Pressure, C_P at $\alpha = 19.98°$ for the different grid levels as well as for curvilinear WMLES.

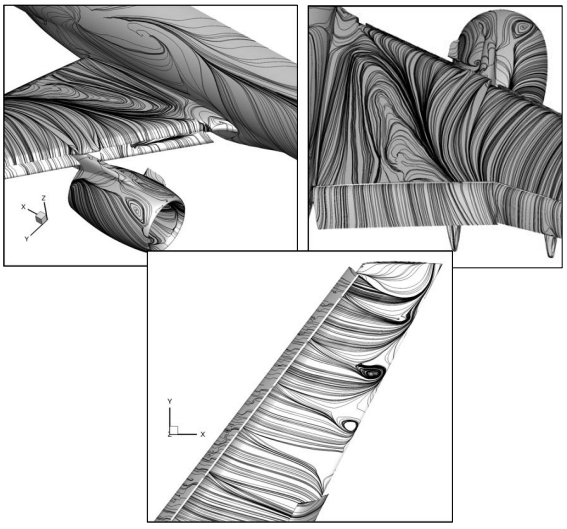

(a) Cartesian WMLES (3mm Grid)

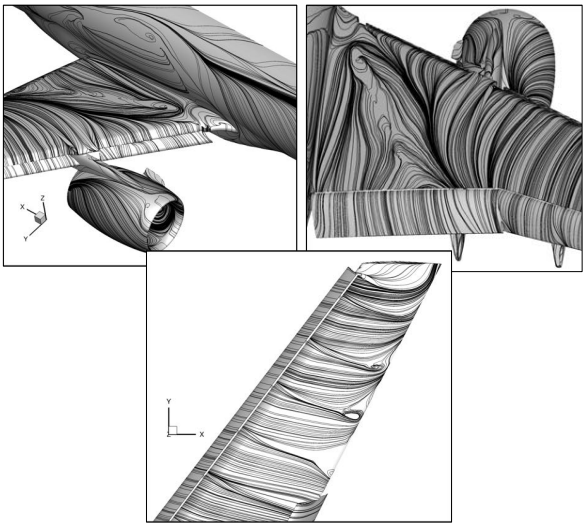

(b) Curvilinear WMLES

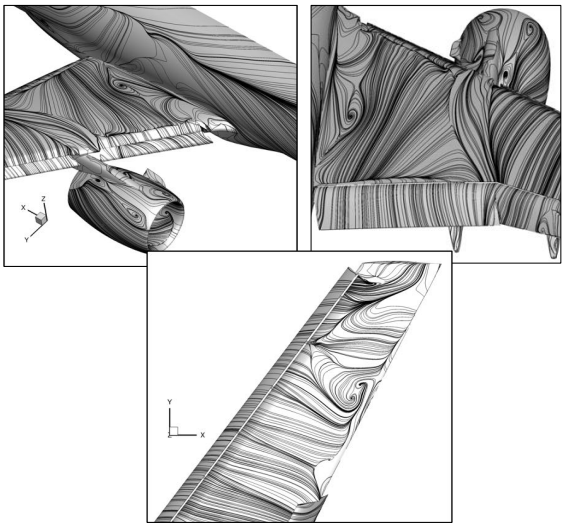

(c) RANS

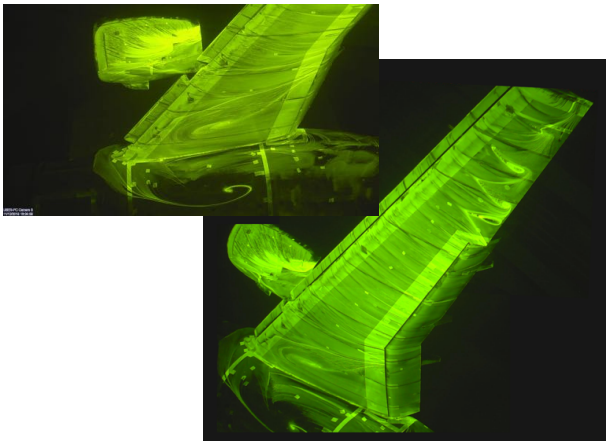

(d) Oil Flow

Fig. 20 Surface Flow Topology at $\alpha = 19.98°$ from WMLES and RANS compared with Oil Flow Imagery from the QinetiQ tunnel experiments[12, 34] (`https://hiliftpw.larc.nasa.gov`)

IV. Role of the tunnel side-walls and standoff

The numerical experiments studied in this section are a consequence of two peculiar observations made using WMLES:

1) **Onset of stall in free-air configuration**: Our previous curvilinear WMLES studies in the free-air[3] configuration showed onset of wing-root separation at 21.48° angle of attack - resulting in a weak pitch break between $\alpha = 20.5°$ and $\alpha = 21.47°$. Each level of grid refinement (performed from 250M grid points through 1.1B grid points) showed a weaker pitch break with pitching moment at $\alpha = 21.47°$ progressively trending nose-up with every level of refinement. However, every grid level showed onset of inboard (corner-flow) separation at 21.47°. This can be seen in the instantaneous c_{fx} surface contours shown in Figures 21c and d. Remarkably, the cartesian WMLES at both 3mm and 4mm grid levels fail to predict onset of such corner flow separation. Instead, these simulations show a boundary layer weakness emanating from the inboard side of the wing-pylon attachment that is larger than any weakness observed in the wing-body juncture. As such the two cartesian simulations do not show a progressively growing corner flow separation bubble in free air in the vicinity of $\alpha = 21.47°$. The two completely different topologies are reminiscent of the finding from the HLPW4-WMLESLB Technical focus group[35] where two flow-topologies were identified with some participants showing onset of corner flow separation (such as the curvilinear WMLES) while other participants showed a more dominant boundary layer weakness downstream of the pylon-wing attachment. However, for in-tunnel simulations the particants obtained similar stall onset mechanisms with a single flow-topology obtained that was in excellent agreement with the QinetiQ experiments. This is similar to the finding described in the previous section - both Cartesian and curvilinear formulations predict an essentially identical stall state. Interestingly, Evans et al. (2020)[11] note the existence of the two distinct flow topologies in tunnel experiments: comparing observations from the Langley 14x22 tunnel and the QinetiQ tunnel. An independent investigation by Koklu et al. (2021)[36] in the Langley 14x22 tunnel studied the effect of the chine vortex on the Nacelle-Pylon vortex structure; their research revealed that the chine vortex plays the role of diminishing the total pressure loss via the Nacelle-Pylon vortex system and mitigating the boundary layer weakness observed downstream of the pylon-wing attachment. Lacy et al. (2020)[34] make an important observation via a combination of tunnel tests and CFD: the nacelle design employed on the QinetiQ and the Langley 14x22 tunnels is sub-optimal for CLmax studies since the nacelle separation onset occurs at around the same angle of attack as the wing-stall. Future tests of HL-CRM will use a modified nacelle design delaying the onset of nacelle lip separation to higher angles of attack. Meanwhile, in the absence of full-span sting mounted experiments for the NASA HL-CRM, it is unclear why the two distinct flow topologies are observed in free-air LES, and as such no concrete judgement regarding correctness of either flow topology can be made at this time. We note that observation of such two distinct topologies is not exclusive to WMLES - both RANS[37] and HRLES[38] show two distinct topologies depending on the use of Rotation-Curvature (RC) and Quadratic constitutive relation (QCR) corrections with the Spalart Allmaras (SA) closure.
2) **Importance of accurate modeling of tunnel boundary layers**: In a previous study we performed two distinct in-tunnel WMLES with viscous (tunnel floor boundary layer) and inviscid (slip-wall) treatments using curvilinear grids[3]. The simulations where tunnel-wall boundary layers developed (viscous boundary treatments), resulted in earlier onset of inboard-stall, roughly occurring at a 1° lower angle of attack. This is shown in Figure 22. This finding appears to be consistent with the experiments by Evans et al. (2020)[11] where use of wall-blowing to recover the the loss of near-wall total pressure resulted in a delayed onset of inboard stall.

Both the observations noted above allude to an epistemic uncertainty in regards to an understanding on stall-onset mechanisms that occur in half-model testing. Three-distinct attributes separate free-air simulations from in-tunnel simulations of half-span geometries:

1) **Blockage effects**: The kinematic blocking of the flow by the tunnel-walls can be interpreted as free-air simulations with mirrored test articles about the tunnel walls. While tunnel-specific corrections can be proprietary, modeling of such wall-interference effects has a rich-history[39] and we will assume that the mapping between the in-tunnel and free-air equivalent angles of attack adequately captures this specific attribute.
2) **Effect of the Standoff**: Side-wall mounted half-span models utilize a peniche/standoff which lifts the relevant parts of the test article away from the tunnel-sidewall boundary layers. However, this standoff introduces a change in the model aspect ratio thereby affecting the spanwise distribution of downwash[40, 41]. It is unclear whether the tunnel corrections account for this effect.
3) **Effect of the floor boundary layer**: The viscous interaction between the tunnel-floor boundary layer and the fuselage/standoff (juncture flow) results in formation of a horse-shoe vortex that can alter the incident angle of

(a) Cartesian 4mm Grid (1100M) (b) Cartesian 3mm Grid (2021M) (c) Curvilinear Grid W-B (360M) (d) Curvilinear Grid W-D (1100M)

Fig. 21 Instantaneous skin friction (c_{fx}) contours comparing two Cartesian WMLES simulations with the curvilinear WMLES simulation for the free-air configuration at $\alpha = 21.47°$.

attack[41–44].

In this section, we formulate certain numerical experiments to study the impact of items 2 and 3 above in a separated manner. The 4mm (1.1B grid point) cartesian mesh is utilized throughout since it offers a good compromise between accuracy and computational cost. Simulations are performed on 4 free-air (corrected) angles of attack for 4 distinct cases:

1) **Baseline**: These are free-air cases of the semi-span model with a symmetry plane specified at $y = 0$m.
2) **With Standoff**: These cases are essentially equivalent to the free-air cases, but the symmetry plane is moved further away from the fuselage to $y \approx -0.8$m since it is now mounted on a standoff.
3) **With Standoff + Thin BL**: In these cases, the symmetry plane at $y \approx -0.8$m is replaced with a viscous wall. The boundary layer of thickness approximately $0.8m$ at the fuselage nose is generated. This floor boundary layer thickness closely represents the boundary layer thickness as characterized by the rake data in QinetiQ experiments.
4) **With Standoff + Thick BL**: But utilizing a roughness patch, the incident floor boundary layer is thickened to approximately 1.5m.

Figure 23 illustrates the problem setup. Figure 24 shows the incident flow seen by the model on a YZ plane - the differences between the two simulated floor boundary layers are abundantly clear - the *thickBL* case has a floor boundary layer that is roughly twice as thick as the *thinBL*. Curvilinear free-air WMLES performed on grid W-B and W-D are utilized throughout to facilitate comparisons between the Cartesian and curvilinear WMLES. Several fascinating observations follow:

1) We begin the technical discussion by considering the flow at 7.05° - the lowest angle of attack studied. Figures 25 and 26 show the surface streamlines comparing the four test cases. Little sensitivity is seen globally, although some minor differences with the inboard flap separation can be noted. The three cases utilizing the standoff appear to show slightly larger inboard flap separation. The pressure coefficients at the inboard station A shown in Figure 30a show slight increase in the inboard suction peak on the main-element which leads to slight increase in C_L (see Figure 31). However, the changes in the integrated loads are not particularly significant to merit deeper analysis.
2) More obvious sensitivities are observed for $\alpha > 19.5°$. The surface streamlines shown in Figure 27 clearly differentiate the two floor BL cases from the baseline and the standoff case. While the effect of the standoff is not entirely clear in the surface streamlines, the total drag shown in Figure 31 clearly demonstrates a reduction due the presence of the standoff. The phenomenological explanation for this reductions is straightforward - the increased distance between the wing-tip vortex and its symmetric counterpart leads to an increase in incident angle of attack, most notably on the inboard parts of the wing. This leads to a reduction in induced drag along with a slight increase in lift. The slight increase in lift due to presence of the standoff can be observed in terms of the increased suction peak in the cp plot in Figure 30b (at Station A). Interestingly, the case with the thin floor BL appears to result in boundary layer weakness in the wing-body juncture - this is evident in both the surface streamlines (Figure 27c) and the inboard suction peaks (Figure 30b). The fourth case with a thick BL, in fact, results in the onset of corner flow separation at $\alpha = 19.57°$ leading to a massive loss of inboard suction (Figure

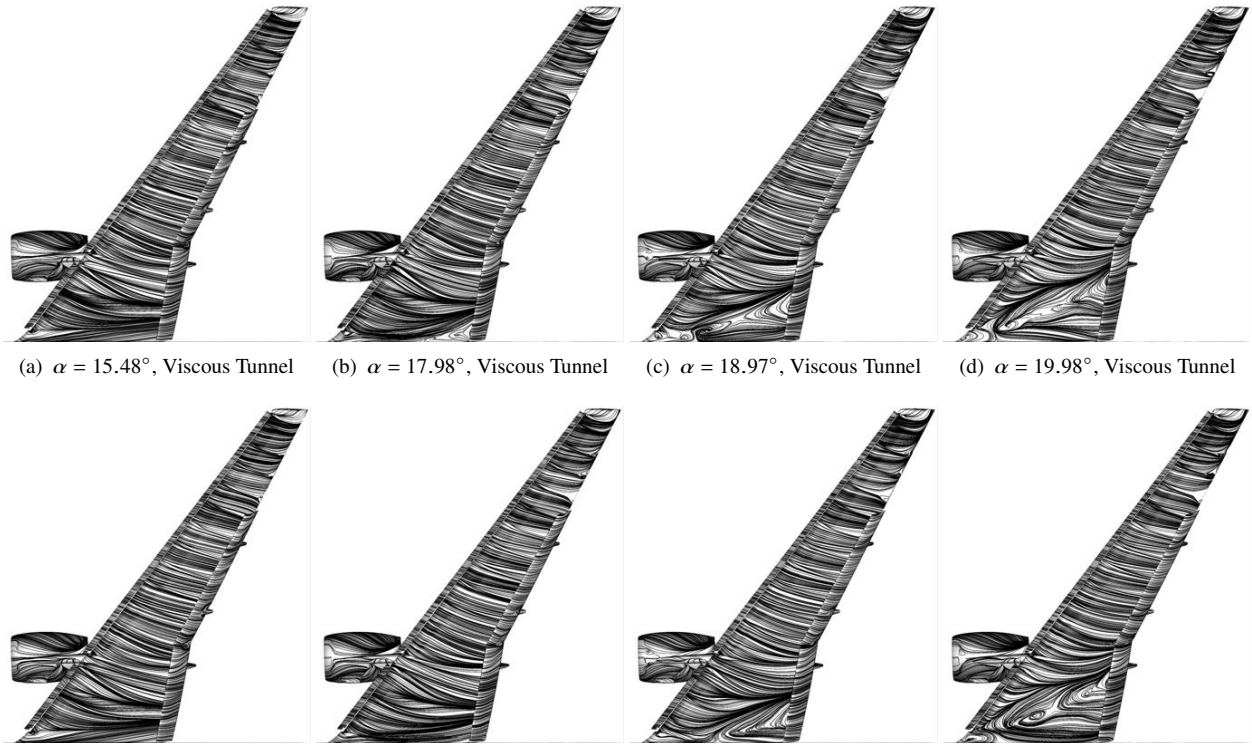

(a) α = 15.48°, Viscous Tunnel (b) α = 17.98°, Viscous Tunnel (c) α = 18.97°, Viscous Tunnel (d) α = 19.98°, Viscous Tunnel

(e) α = 15.48°, Inviscid Tunnel (f) α = 17.98°, Inviscid Tunnel (g) α = 18.97°, Inviscid Tunnel (h) α = 19.98°, Inviscid Tunnel

Fig. 22 Effect of the tunnel wall boundary layer on the inboard stall mechanism as predicted using Curvilinear WMLES (360M grid).

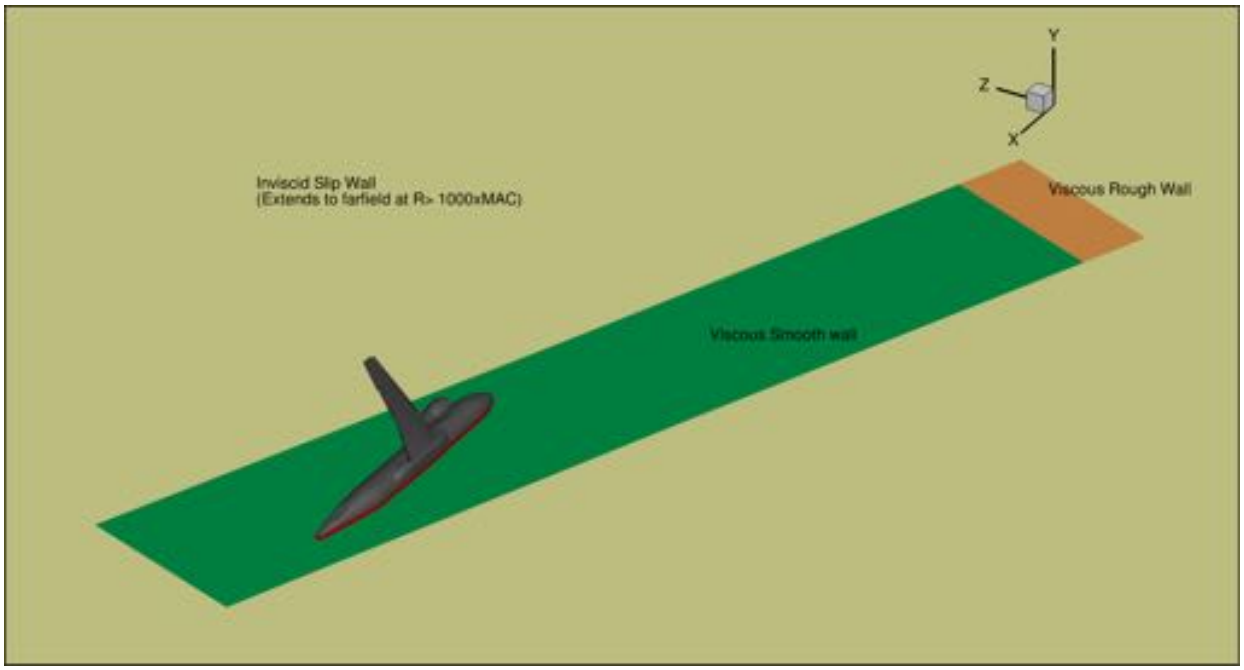

Fig. 23 Schematic illustrating the simulation setup to study the effect of floor boundary layer.

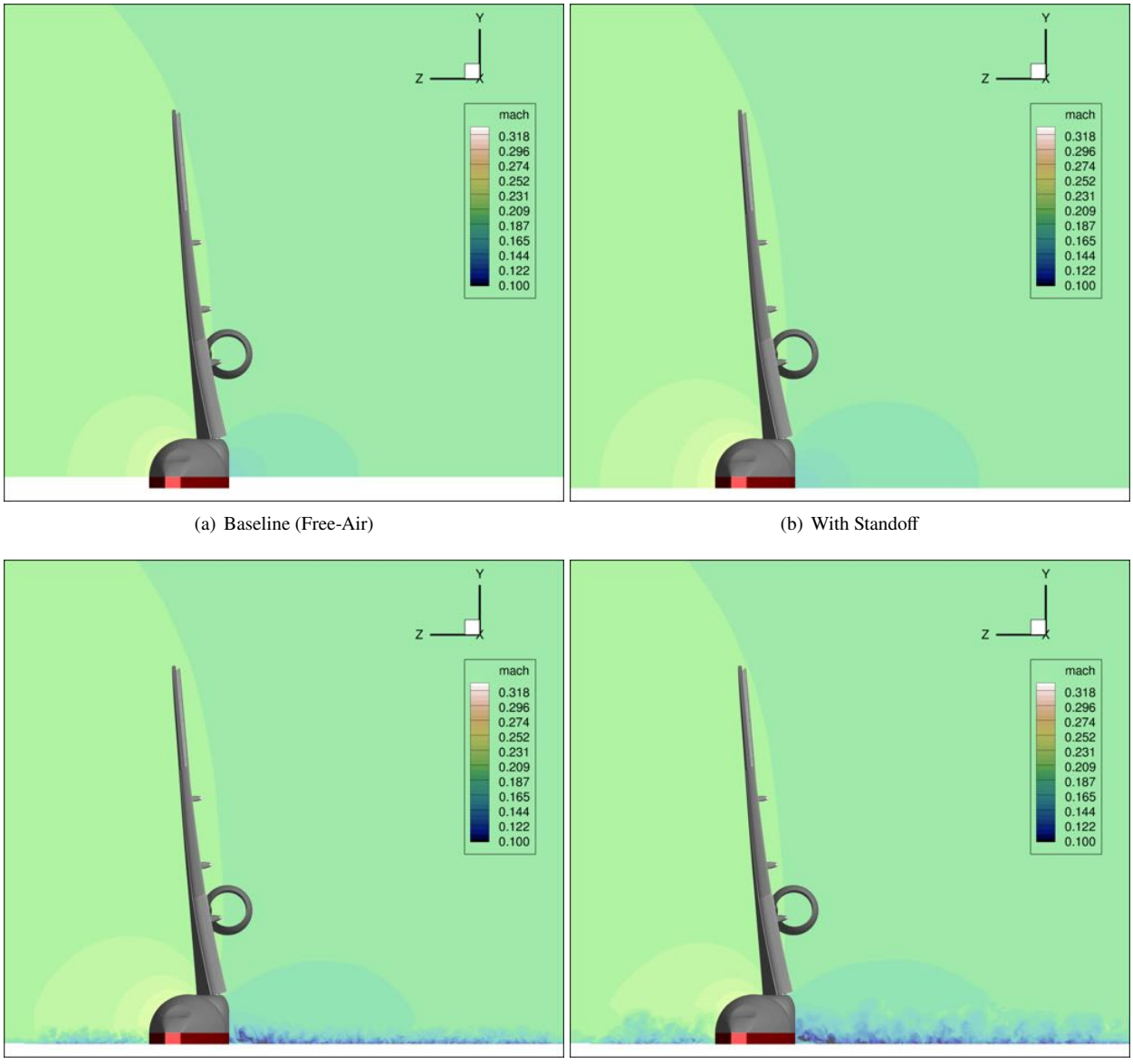

(a) Baseline (Free-Air)

(b) With Standoff

(c) With Standoff + Thin BL

(d) With Standoff + Thick BL

Fig. 24 Instantaneous Mach number on the YZ plane taken as $x = 7$m plane - showing the differences between the 4 cases studied.

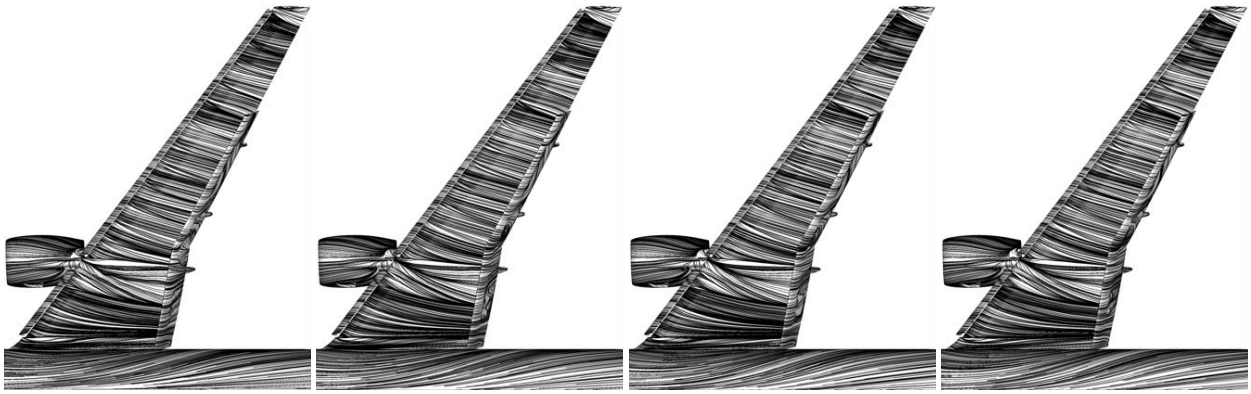

(a) Baseline (Free-Air) (b) With Standoff (c) With Standoff + Thin BL (d) With Standoff + Thick BL

Fig. 25 Surface skin-friction streamlines at $\alpha = 7.05^\circ$ on the 4mm (1100M) Cartesian Grid

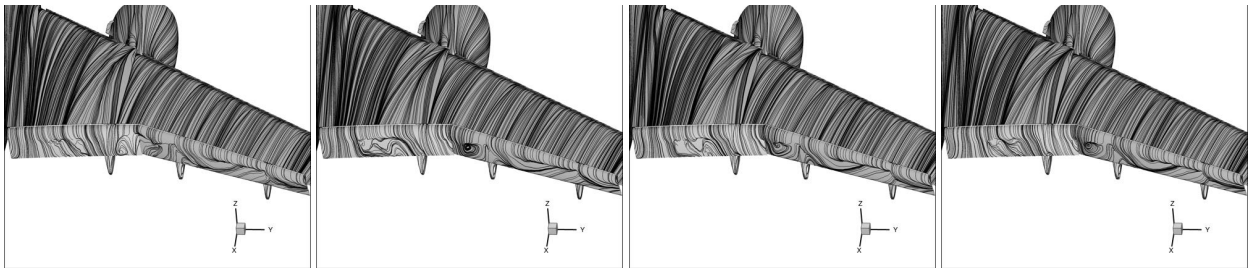

(a) Baseline (Free-Air) (b) With Standoff (c) With Standoff + Thin BL (d) With Standoff + Thick BL

Fig. 26 Surface skin-friction streamlines on the flap $\alpha = 7.05^\circ$ for the 4mm (1100M) Cartesian Grid

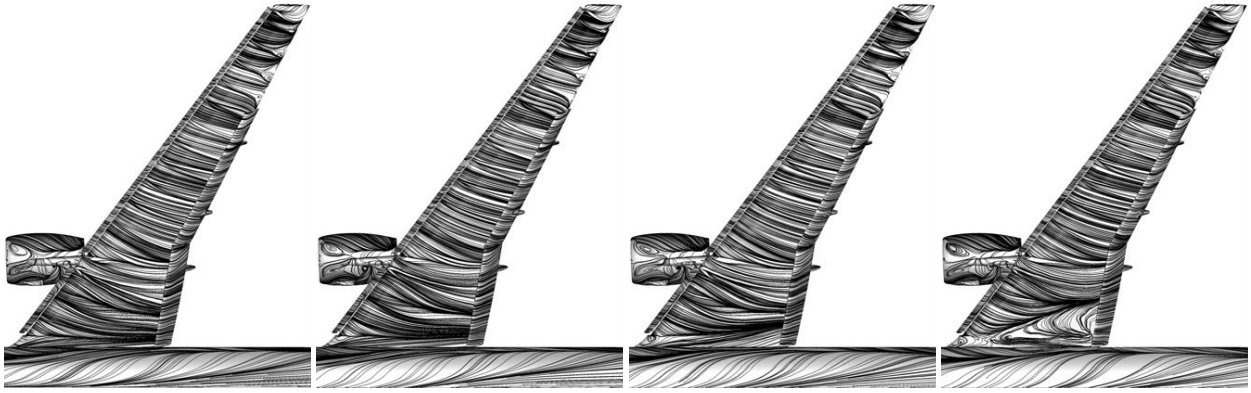

(a) Baseline (Free-Air) (b) With Standoff (c) With Standoff + Thin BL (d) With Standoff + Thick BL

Fig. 27 Surface skin-friction streamlines at $\alpha = 19.57°$ on the 4mm (1100M) Cartesian Grid

30b). Hence, we conclude that while the standoff does alter inboard flow, the larger leading order effect appears to be due to the floor boundary layer. The phenomenological explanation for this behavior will be addressed momentarily.

3) At $\alpha = 21.47°$, both boundary layer cases show strong onset of wing-root separation whereas the two symmetry-plane cases do not (see Figure 28). Remarkably, both the thick and the thin boundary layer cases show surprisingly good agreement with the inboard cp when compared with the corrected experiment data at $\alpha = 21.47°$; the case with the thicker floor boundary layer showed a larger loss of inboard suction (see Figure 30c). An increase in angle-of-attack to $\alpha = 22°$ shows onset of corner flow separation for the case with the standoff as well (see Figure 29), although this separation bubble is only incipient. Thus while there is loss of inboard suction for the case with standoff, it still largely overpredicts the inboard suction compared with the experiment (as well as with the two floor BL cases and the free-air curvilinear cases). However, it is clear that weakness seen in the wing-body juncture is larger than that observed downstream of the pylon attachment when a standoff is modelled in free-air configurations. This indicates that the small increase in apparent angle of attack on the inboard wing is sufficient to cause a change of inboard flow-topology in the Cartesian WMLES. Note that while the curvilinear WMLES does show a loss-of-suction on the inboard wing, the cases with the two floor boundary layers experience a far more dramatic separation and produce a pitch break that is largely consistent with the corrected experimental data (see Figure 31).

4) In order to understand the fundamental difference between the cases with floor boundary layers and the cases with symmetry plane, we now consider constant-X slices (YZ-plane) at various locations shown in Figures 32 and 33. The total pressure coefficient contours show regions where loss-of-total pressure occurs due to generation of vorticity. Comparisons are performed at $\alpha = 19.57°$ since differences between the different cases at $\alpha > 21.47°$ are too large to enable a discussion regarding the phenomenological effects of the floor boundary layer. Data from the curvilinear simulation on grid W-D (1.1B points) is also included for completeness. Several pertinent observations can be made that explain the effect of floor boundary layer on the inboard flow-topology:
   (a) The roll-up vortex that forms on the top side of the fuselage appears to be identical between the baseline Cartesian WMLES and the curvilinear WMLES at all x locations shown. Interestingly, the presence of the standoff does not cause a large change in this fuselage roll-up vortex since it is generated due to curvature change on the fuselage as opposed to the distance from the symmetry plane. The most interesting observation that can be made is the existence of a large corner flow vortex (with the appearance of a horse-shoe when viewed on the XZ plane) that forms on the belly-side of the fuselage in the two cases with the floor boundary layer. This vortex appears to be stronger for the case with the thicker floor boundary layer. The two-dimensional streamlines show that this vortex exists at all x-stations considered starting at $x = 10$m through $x = 37$m and most certainly will affect the spanwise (y-directional) flow seen by the main-element.
   (b) To understand the effect of the belly-side corner-flow vortex on the inboard flow topology, we next consider the apparent angle of attack seen by the model at the $x = 24.55$m plane - just upstream of the

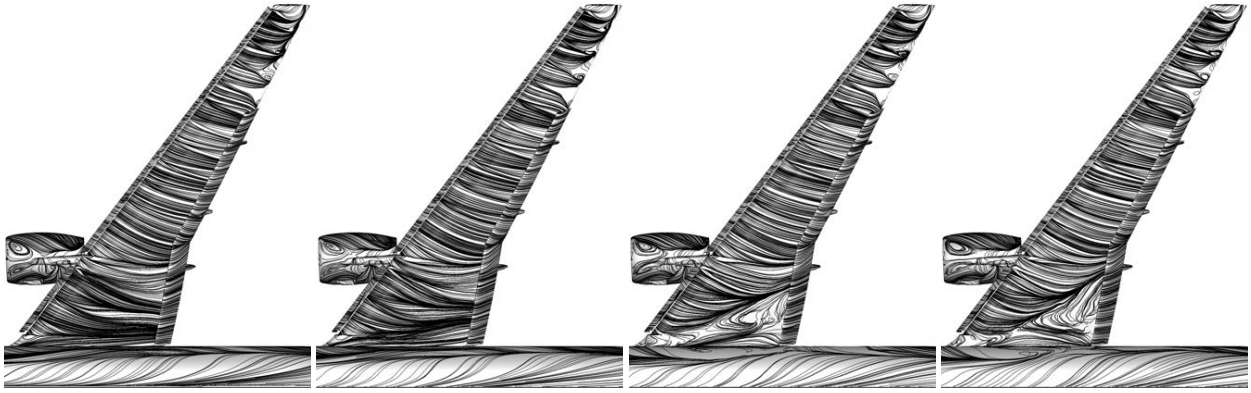

(a) Baseline (Free-Air) (b) With Standoff (c) With Standoff + Thin BL (d) With Standoff + Thick BL

Fig. 28 Surface skin-friction streamlines at $\alpha = 21.47°$ on the 4mm (1100M) Grid

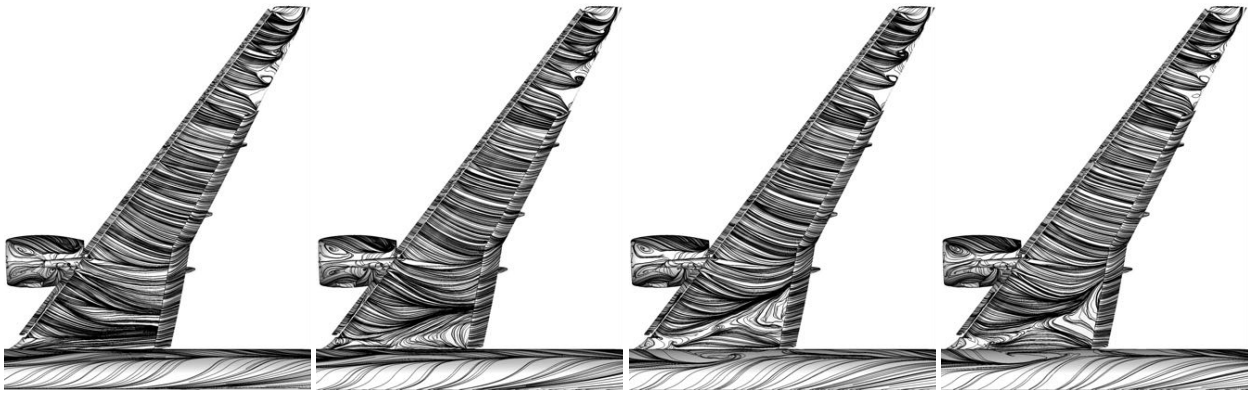

(a) Baseline (Free-Air) (b) With Standoff (c) With Standoff + Thin BL (d) With Standoff + Thick BL

Fig. 29 Surface skin-friction streamlines at $\alpha = 22.00°$ on the 4mm (1100M) Grid

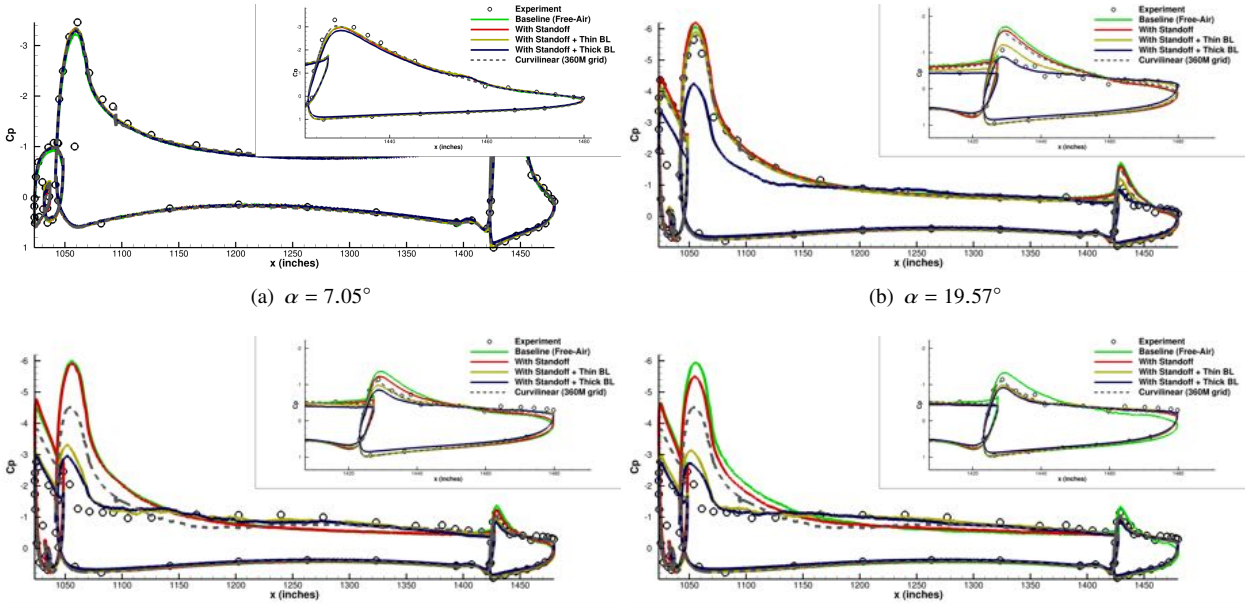

(a) $\alpha = 7.05°$ (b) $\alpha = 19.57°$

(c) $\alpha = 21.47°$ (d) $\alpha = 22.00°$

Fig. 30 Coefficient of Pressure, C_P at Station A ($\eta = 0.15$ for varying angles.)

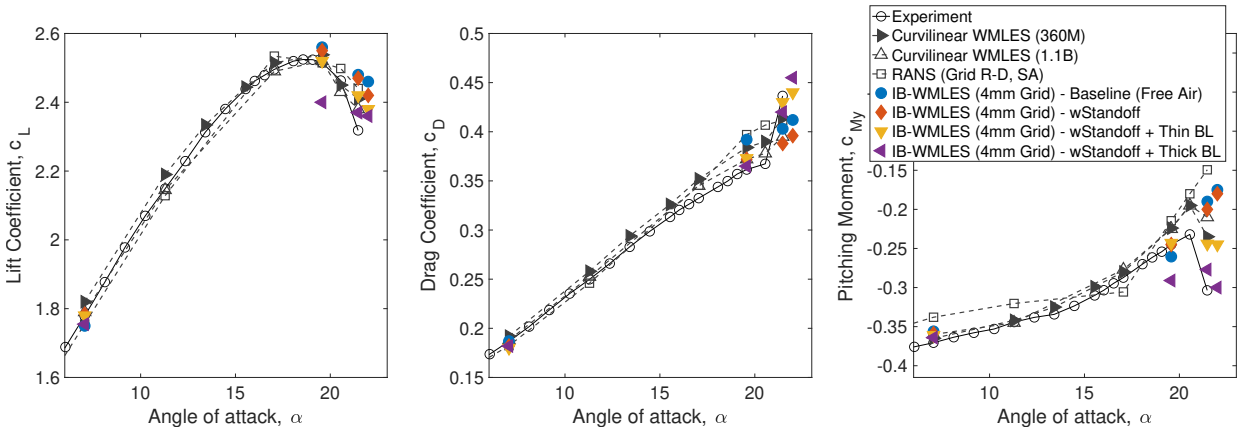

Fig. 31 Integrated forces and moments for free-air simulations with varying wall-treatments.

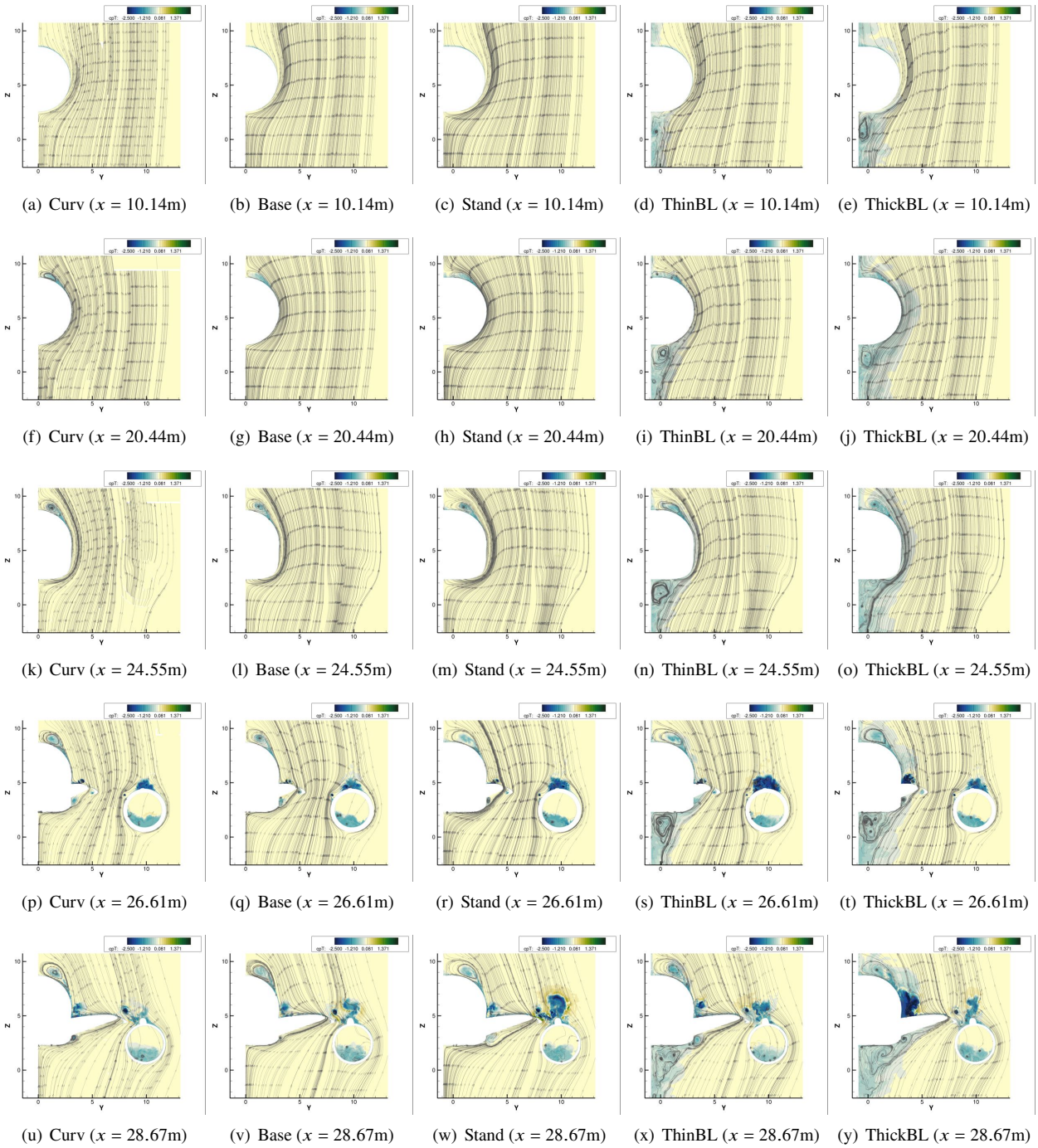

(a) Curv (x = 10.14m) (b) Base (x = 10.14m) (c) Stand (x = 10.14m) (d) ThinBL (x = 10.14m) (e) ThickBL (x = 10.14m)

(f) Curv (x = 20.44m) (g) Base (x = 20.44m) (h) Stand (x = 20.44m) (i) ThinBL (x = 20.44m) (j) ThickBL (x = 20.44m)

(k) Curv (x = 24.55m) (l) Base (x = 24.55m) (m) Stand (x = 24.55m) (n) ThinBL (x = 24.55m) (o) ThickBL (x = 24.55m)

(p) Curv (x = 26.61m) (q) Base (x = 26.61m) (r) Stand (x = 26.61m) (s) ThinBL (x = 26.61m) (t) ThickBL (x = 26.61m)

(u) Curv (x = 28.67m) (v) Base (x = 28.67m) (w) Stand (x = 28.67m) (x) ThinBL (x = 28.67m) (y) ThickBL (x = 28.67m)

Fig. 32 Stagnation pressure coefficient contours at various x locations along with two-dimensional planar streamlines on YZ plane. Solutions compared at $\alpha = 19.57°$.

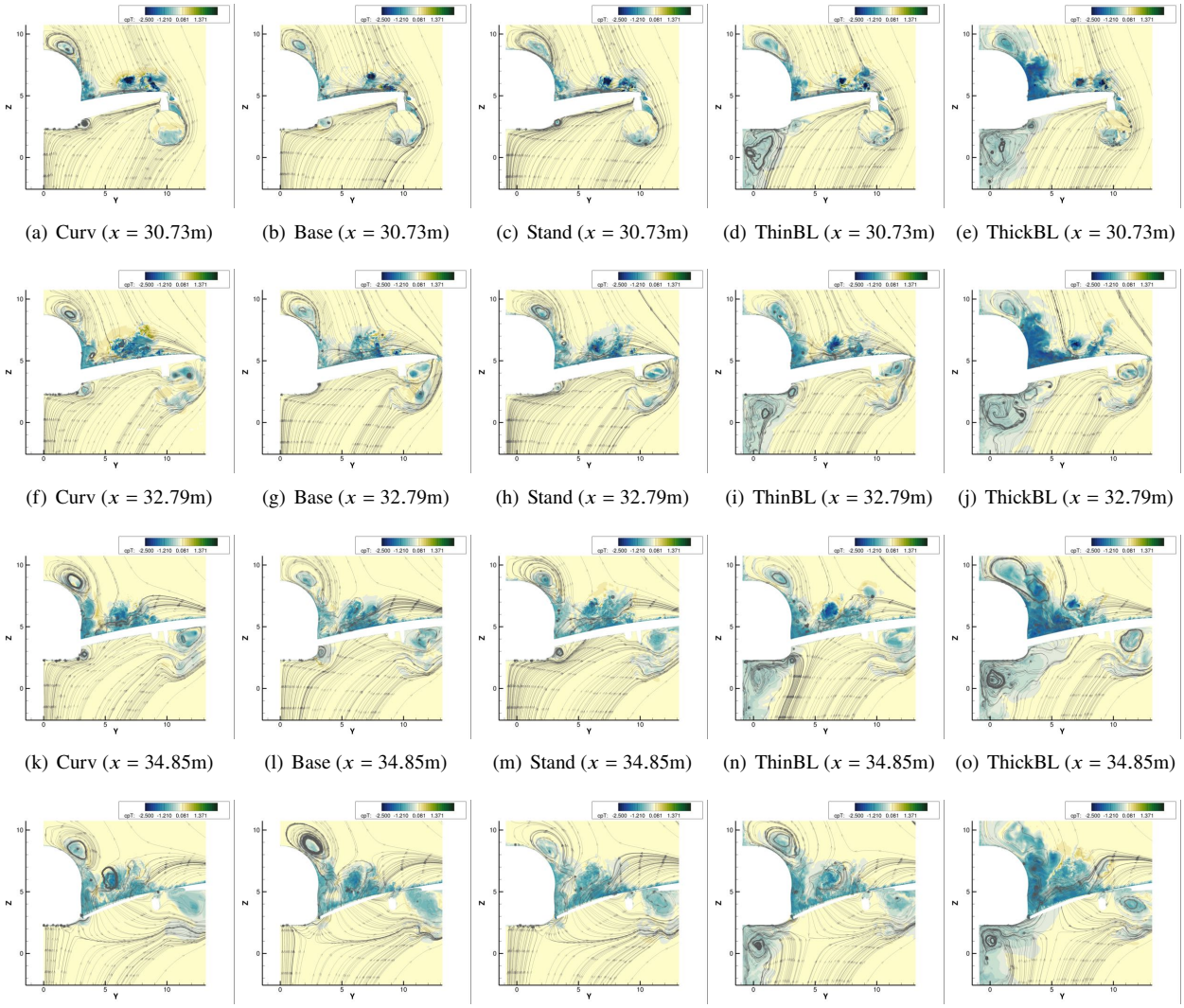

(a) Curv (x = 30.73m) (b) Base (x = 30.73m) (c) Stand (x = 30.73m) (d) ThinBL (x = 30.73m) (e) ThickBL (x = 30.73m)

(f) Curv (x = 32.79m) (g) Base (x = 32.79m) (h) Stand (x = 32.79m) (i) ThinBL (x = 32.79m) (j) ThickBL (x = 32.79m)

(k) Curv (x = 34.85m) (l) Base (x = 34.85m) (m) Stand (x = 34.85m) (n) ThinBL (x = 34.85m) (o) ThickBL (x = 34.85m)

(p) Curv (x = 36.91m) (q) Base (x = 36.91m) (r) Stand (x = 36.91m) (s) ThinBL (x = 36.91m) (t) ThickBL (x = 36.91m)

Fig. 33 Continued from previous figure - Stagnation pressure coefficient contours at various x locations along with two-dimensional planar streamlines on YZ plane. Solutions compared at α = 19.57°.

leading edge strake. This is shown in Figure 34. It is clear that both the curvilinear WMLES and the baseline (free-air) Cartesian WMLES on the 4mm grid show essentially identical incidence angles of attack. However, the case with the standoff appears to have slightly higher angle of attack throughout the portion of the wing between the fuselage and the nacelle. This is consistent with the arguments relating to altered downwash made earlier. More interestingly, the two cases with the floor boundary layer clearly show a substantially higher effective angle of attack at the leading-edge strake. This is confirmed by looking at the constant Y slice (on the XZ plane) at $y = 3.15$m (see Figures 35a-e). The flow angularity change due to presence of the belly-side corner-flow vortex in the two cases with the floor BL is illustrated by the red-arrows tangent to the local flow. This increased angle of attack near the wing-root is likely responsible for the onset of corner-flow separation in the Cartesian WMLES.

(c) The differences between the 5 cases studied essentially vanish further outboard as seen in Figures 35(k) through (t).

5) Finally comparisons of the surface-flow streamlines obtained for the baseline Cartesian WMLES and the curvilinear WMLES are shown in Figure 36. Reasonable agreement is seen between the two - although the curvilinear solution does show large outboard movement of the stream in the wing-body juncture compared to the Cartesian WMLES. We will refer to this outboard movement of the streamline as - showing a large tendency to form corner-flow separation. By comparing the curvilinear WMLES streamlines in Figure 36 with the streamlines for the other three Cartesian configurations studied, we can rank the five simulations in terms of their respective tendencies for wing-root (corner-flow) separation:

   (a) Cartesian WMLES of the baseline (free-air) configuration shows the least tendency for corner-flow separation. In fact this case does not show any onset of wing-root separation even at $\alpha = 22°$ - the streamlines do not show any outboard shift with increasing angles of attack (see Figures 27a - 29a).

   (b) Cartesian WMLES of the standoff configuration shows a slightly larger tendency for corner-flow separation. This is likely due to an increased inboard angle of attack as seen in Figure 27b. Interestingly unlike the baseline Cartesian WMLES, the cases with a standoff continue to show an increasing tendency for wing-root separation with increasing angle of attack (see Figures 27b - 29b). Eventually onset of wing root separation occurs at $\alpha - 22°$. This is consistent with the claim made previously - inclusion of the standoff in these unconfined simulations is sufficient to trigger a switch in the inboard flow topology.

   (c) Curvilinear WMLES on the 1.1B point grid W-D shows a slightly higher tendency for wing-root separation (see Figure 36a) compared to the Cartesian WMLES with Standoff. This case eventually shows an onset of corner-flow separation at $\alpha = 20.55°$ (as was shown in [3]).

   (d) Cartesian WMLES with the thin floor boundary layer shows a substantially larger tendency for corner-flow separation compared to the previous three-cases (see Figure 27c). This case most likely will show onset of wing-root separation at $\alpha < 20.5°$.

   (e) Cartesian WMLES with a thick floor boundary layer shows wing root separation at $\alpha = 19.57°$ itself (see Figure 27d).

   The increasing tendency for wing-root separation between the baseline Cartesian WMLES and the standoff Cartesian WMLES is consistent with the increased inboard angle of attack. Similarly the further increase in this tendency due to the floor boundary layers is also consistent with the further increase in incident angle of attack at the leading edge strake due to the presence of the fuselage belly-side vortex. This leads to the important question: *What is the cause of the difference between the baseline Cartesian WMLES and the baseline Curvilinear WMLES?*

6) One potential explanation is the Nacelle-lip separation. In Figure 34, it is evident that primary differentiation between the Curvilinear WMLES and the four Cartesian WMLES is the incident angle of attack just upstream of the Nacelle. This appears to be a non-local (upstream) effect of larger Nacelle lip separation seen in the cartesian cases compared to the curvilinear case. It is possible that the larger loss-of-total pressure on the Nacelle lip (and subsequently in the Nacelle-Pylon vortex) in the Cartesian WMLES (see Figures 35p-t) along with the interplay between the chine-vortex and the Nacelle-Pylon vortex could provide an explanation for the difference between the two topologies. At this time, we do not think that the difference has to do with grid resolution differences between the two - Figure 37 compares the chine-vortex specific refinements employed in the two grid systems. Both grids have similar resolutions in their respective chine refinement blocks.

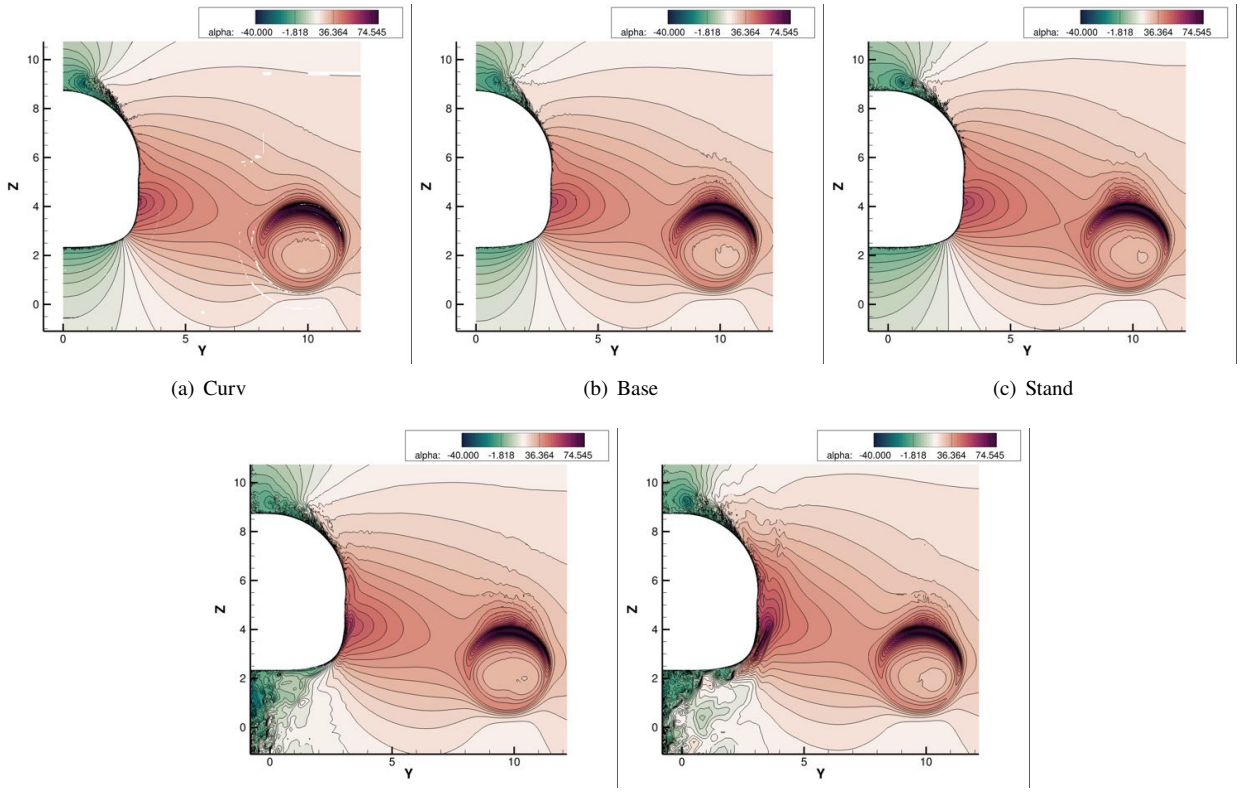

(a) Curv (b) Base (c) Stand

(d) ThinBL (e) ThickBL

Fig. 34 Incidence angle of attack at $x = 24.55$m plane - just upstream of the leading-edge strake. Solutions compared at $\alpha = 19.57°$. Angle contours shown are in degrees.

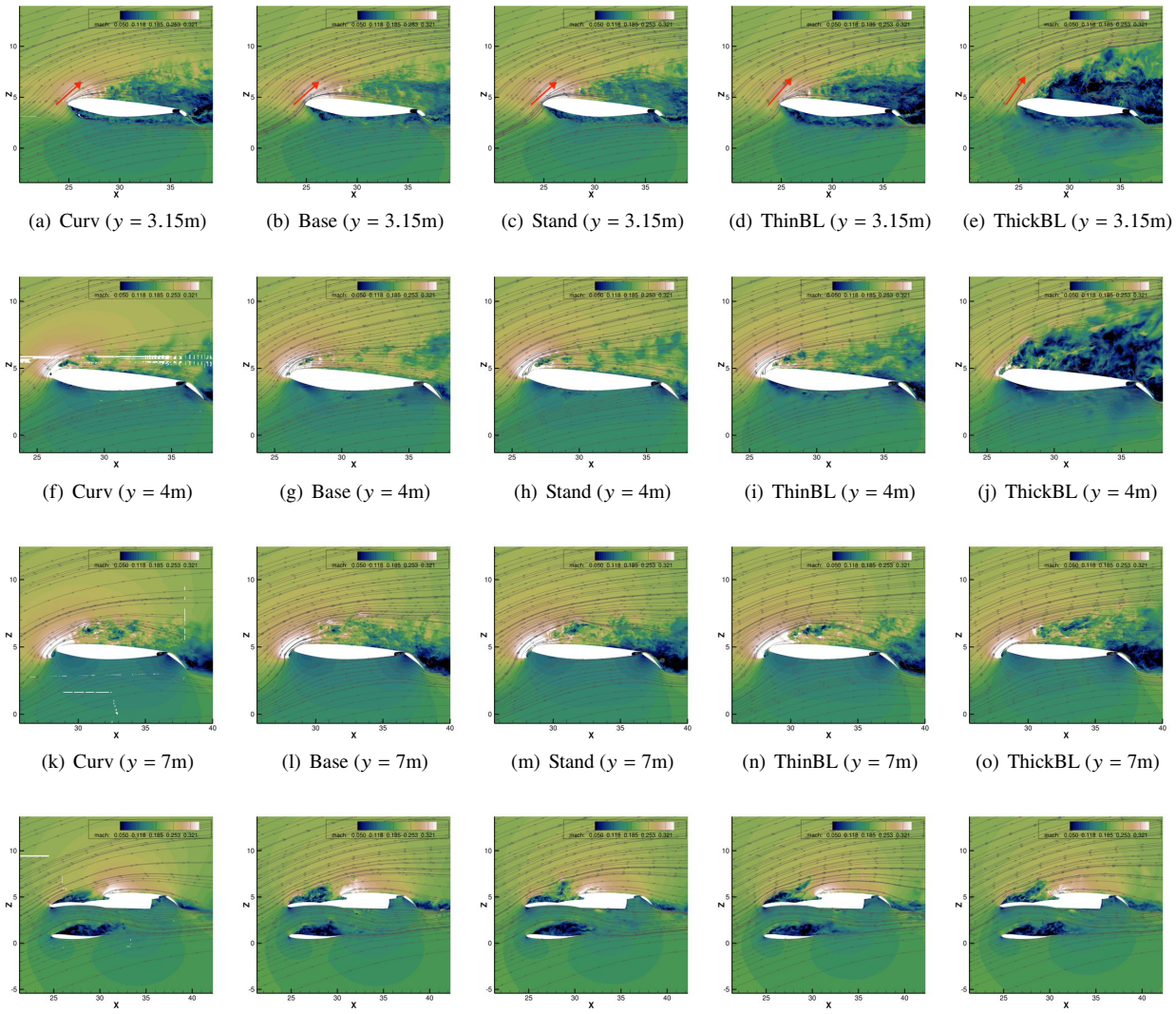

(a) Curv (y = 3.15m) (b) Base (y = 3.15m) (c) Stand (y = 3.15m) (d) ThinBL (y = 3.15m) (e) ThickBL (y = 3.15m)

(f) Curv (y = 4m) (g) Base (y = 4m) (h) Stand (y = 4m) (i) ThinBL (y = 4m) (j) ThickBL (y = 4m)

(k) Curv (y = 7m) (l) Base (y = 7m) (m) Stand (y = 7m) (n) ThinBL (y = 7m) (o) ThickBL (y = 7m)

(p) Curv (y = 10m) (q) Base (y = 10m) (r) Stand (y = 10m) (s) ThinBL (y = 10m) (t) ThickBL (y = 10m)

Fig. 35 Mach number contours on various XZ slices along with two-dimensional streamlines on a constant Y plane.

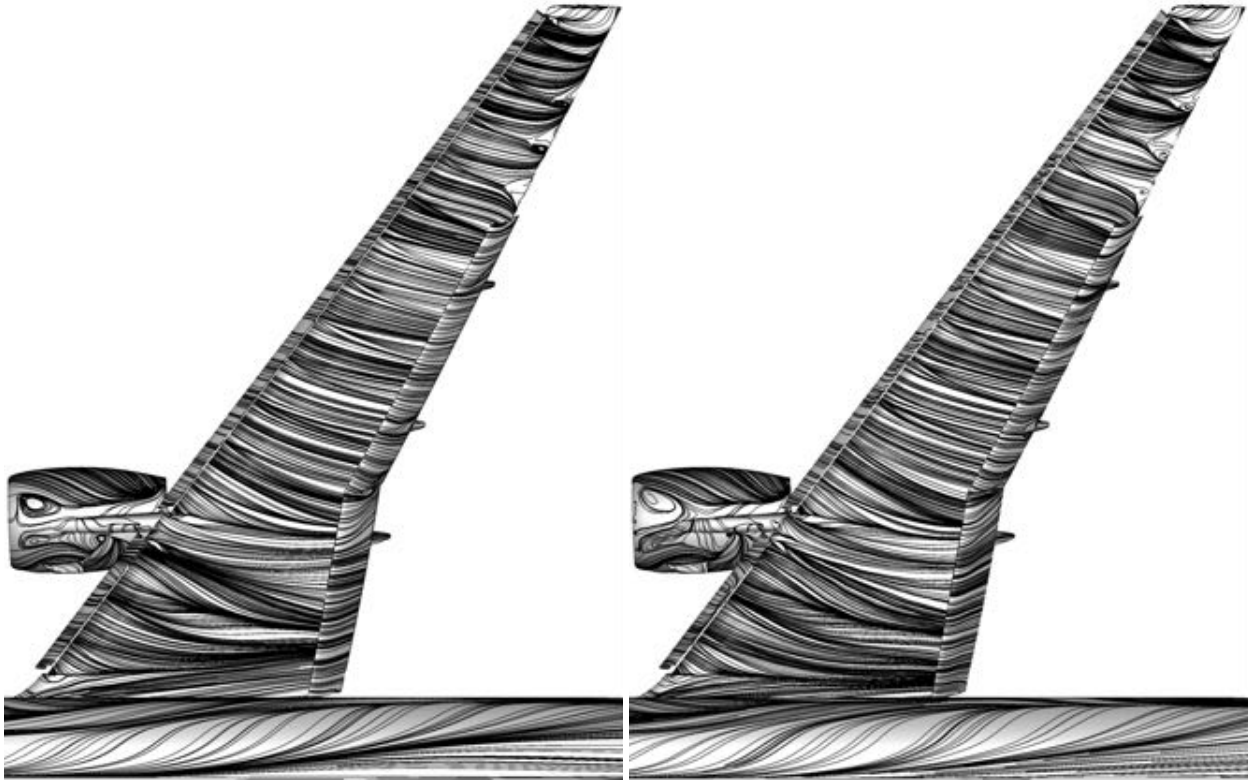

(a) Curvilinear WMLES, 1100M - Grid W-D

(b) Cartesian WMLES (Baseline), 4mm 1100M point grid

Fig. 36 Chine vortex refinement grids compared between curvilinear and the 4mm Cartesian grid (baseline) at $x = 34.85$m.

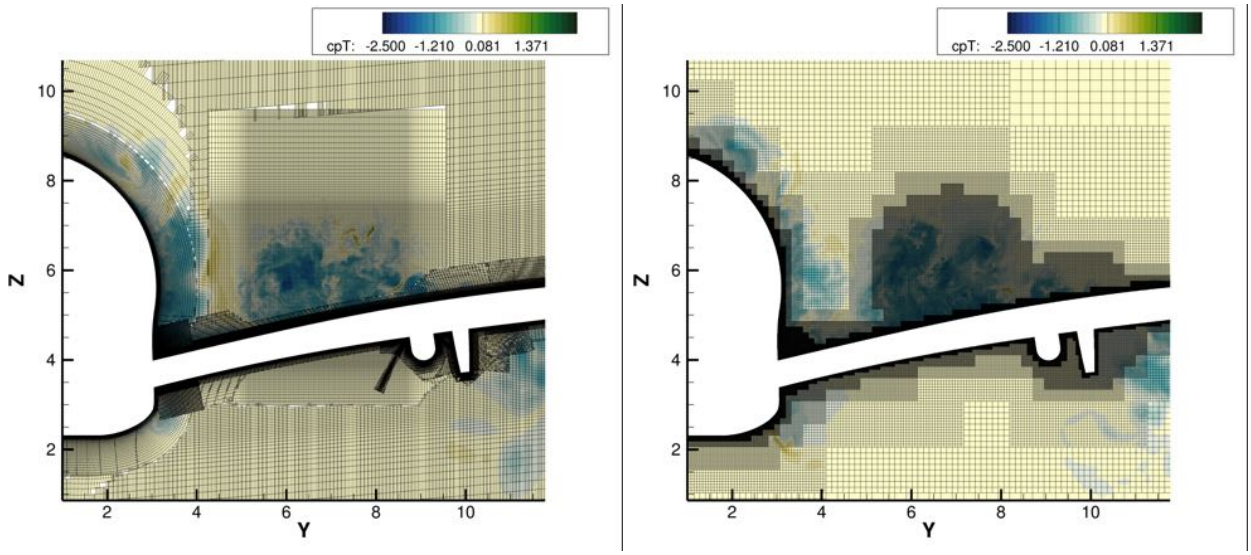

(a) Curvilinear (1100M - Grid W-D)

(b) Baseline Cartesian (4mm, 1100M grid)

Fig. 37 Chine vortex refinement grids compared between curvilinear and the 4mm Cartesian grid (baseline) at $x = 34.85$m.

V. Computational Cost

Computational cost requirements for the new immersed boundary WMLES formulation compared against curvilinear grid WMLES and curvilinear grid RANS data (presented in Kiris et al. (2022)[3]) are given in Table 2. Note that we do not include the 12mm, 100M grid costs in the table since we do not believe the results for that grid are objectively more accurate than steady state RANS results. All three Cartesian Octree grids shown here produce more accurate in-tunnel results than steady state RANS. Some remarks discussing the relative computational costs follow:

1) A key enabler for utilization of Cartesian overset grids is the lower algorithmic complexity due to lack of metric terms and associated memory and computational overheads. The computational cost per degree-of-freedom is approximately 2 times higher in Curvilinear grids compared to Cartesian grids. This is particularly relevant since due to the unity aspect ratio enforcement in Cartesian Octree topologies a substantially larger number of grid points is needed to obtain the same wall-normal resolutions as the curvilinear grids. WMLES of wall-bounded flows (especially in equilibrium attached flows) can accurately capture skin-friction on wings using grid with aspect ratios as high as 6[17]. This enables a substantial reduction in surface degrees of freedom needed in curvilinear grids on large portions of the geometry where primarily equilibrium wall-turbulence is seen (pressure-side of lifting surfaces, fuselage, etc).
2) Perfectly isotropic grids utilized in the Cartesian formulation enable the use of highly efficient explicit time-step discretizations (such as the RK3 scheme[31] used in the present study) since the moderate compressiblity effects are expected for the present problem (outboard slats experience nearly sonic conditions at high angles of attack). Explicit time-stepping schemes are also very lucrative for the curvilinear formulation, however very careful grid generation is needed to avoid poor quality grids cells - this is a very human-intensive and tedious task.
3) While the 3mm grid resolution was needed to obtain results with similar accuracy as the curvilinear grid WMLES, we note that refinements performed in the current work were overly conservative. This was done to ensure a consistent grid refinement study - we are quite confident that similar accuracy results can be obtained using grids with targeted grid refinements thereby substantially reducing the total grid points. However, it is still promising to note that the simulations on the 2 Billion grid point Cartesian octree grid are only about 2.8x more expensive than the simulations on the 360M point curvilinear grid.
4) Cost numbers presented in Table 2 reflect the relative cost of WMLES compared to steady-state RANS on structured overset grids. It is clear that accurate WMLES is likely to be at least 10x more expensive than representative RANS simulations. However, we emphasize that WMLES using explicit-time step discretizations are highly suitable for modern computational architectures that rely on accelerators such as GPUs. These modern HPC resources can reduce the wall-time for WMLES substantially making it comparable with wall-times for steady-state RANS.
5) Staggering improvements in overall turn-around time are enabled by utilizing cartesian octree grids over curvilinear overset grids. For geometries as complex as the HL-CRM, this paper has demonstrated at least 1-2 month reduction in solution turn-around time by utilizing the new immersed boundary WMLES formulation.

VI. Summary

A comprehensive assessment of the recently developed immersed boundary wall-modelled LES formulation leveraging Cartesian Octree grids was performed to gauge its capability for $C_{L,\max}$ prediction on the NASA HL-CRM. Previously conducted WMLES using curvilinear structured overset grids allowed for some interesting comparisons between the two methodologies. The analysis performed can be summarized succinctly in terms of two distinct themes:

1) **Two distinct flow topologies for free-air simulations**: While the curvilinear and Cartesian WMLES formulation predicted consistent flow topologies for the in-tunnel simulations, this was unfortunately not the case for free-air configuration. While agreement between the two methods was good for $\alpha < 20°$, two distinct inboard flow topologies were observed at $\alpha > 20°$. While the curvilinear simulations showed a weakness in the wing-body juncture region eventually leading to a fully formed wing root separation region at $\alpha = 21.47°$, the Cartesian simulations showed a more prevalent boundary layer weakness emanating downstream from the pylon-wing attachment. While a phenomenological explanation for these difference could not be rigorously established, we postulate four potential causes for these differences:
    (a) Differences in Nacelle lip separation between the curvilinear and Cartesian simulations were very evident with the Cartesian simulations predicting a more dramatic nacelle separation. This leads to a larger loss on total pressure on the Nacelle and the subsequent Nacelle/Pylon vortex that forms further downstream. Since the Nacelle/Pylon and the Chine vortex interact[36] the resulting differences in the overall vortex

Table 2 Computational cost requirements for different simulation methods employed for the High-Lift Common Research Model in the semi-span, free-air configuration. Note that the acronym CTU stands for *Convective time unit* which is a non-dimensionalization based on $u_{\text{ref}}/c_{\text{MAC}}$ and the acronym NAS SBU stands for *NASA Advanced Supercomputing Standard Billing Unit* which is a specific charge rate for each node type as of May, 2022.

Attribute	Simulation Methodology				
	RANS (Steady) Grid R-C	Curv-WMLES Grid W-B	IB-WMLES 6mm, 450M grid	IB-WMLES 4mm, 1100M grid	IB-WMLES 3mm, 2020M grid
Solve Points	223M	360M	450M	1100M	2020M
Timestep size	-	$3.5 \times 10^{-6} s$	$7.4 \times 10^{-6} s$	$4.8 \times 10^{-6} s$	$3.3 \times 10^{-6} s$
Nodes used for benchmark	35 Skylakes (40 cores/node)	100 AMD Romes (128 cores/node)	100 Skylakes (40 cores/node)	100 Skylakes (40 cores/node)	100 Skylakes (40 cores/node)
Core-time per compute point per timestep	-	$2.03 \mu s$	$0.75 \mu s$	$0.75 \mu s$	$0.75 \mu s$
Timesteps per CTU	-	29,338	13,782	21,392	31,116
Core-time per CTU	-	5970 hours	1300 hours	4900 hours	13090 hours
Simulation time needed for $\alpha = 19.57°$	-	50 CTU	50 CTU	50 CTU	50 CTU
Core-time needed for $\alpha = 19.57°$	21,000 hours	298,500 hours	65,000 hours	245,000 hours	654,000 hours
NAS SBUs needed for $\alpha = 19.57°$	**835**	**9,470**	**2,600**	**9,800**	**26,100**
Relative Cost over typical RANS	**1.0**	**11.3**	**3.1**	**11.7**	**31.2**
Grid Generation (Human Effort)	**1-2 months**	**1-2 months**	**2 hours**	**2 hours**	**2 hours**

system on the suction side of the wing seems to be correlated with the BL weakness downstream of the pylon mount. However, at this time a rigorous causal relationship between the two observations cannot be confirmed.

(b) The Cartesian octree-grids are more naturally suited for LES of off-body vorticity which plays a major role especially at higher angles of attack. While an off-body refinement was performed in the curvilinear grids which resulted in a delay in the onset of corner-flow separation, subsequent refinements only increased the resolution within the boundary layers.

(c) It is possible that neither the curvilinear nor the Cartesian simulations were run long enough for persistent topolgies to form. While both simulations were run for at least 70CTU at the highest angle-of-attack, it is possible that longer time-scale transient motions have not been adequately flushed out.

(d) The curvilinear simulations approach a low-C_L attracter (low-C_L branch), and the Cartesian simulations approach a high-C_L attracter (high-C_L branch) for the free-air runs. Without lack of full-span and sting mounted experiments, this discrepancy between the two methods is unlikely to be resolved ;if indeed, the two formulations are approaching two physical solution branches.

2) **Sensitivity to tunnel floor boundary layers**: In order to reconcile the fact that both Cartesian and curvilinear formulations predict identical stall mechanisms for in-tunnel configuration but not for the free-air configuration, a series of systematic numerical experiments were conducted using immersed boundary WMLES. The outcomes were very interesting:

   1) The presence of the standoff was sufficient to trigger a switch in the inboard flow-topology. Unconfined/free-air simulations show that the standoff (which increases the distance between the wing-tip vortex and the symmetry plane) causes a change in the downwash - leading to a drop in drag and an increase in the incident angle of attack near the wing root. This increase in angle of attack near the wing root leads to a substantial increase in BL weakness in the wing-body juncture with onset of corner-flow separation reported at $\alpha = 22^\circ$. This was in stark contrast with the baseline simulations that showed little change in the inboard surface streamlines with α increasing from 19.5° to 22°.

   2) Two additional cases, with a floor boundary layer of varied thickness, were also analysed. Evidence was shown for the existence of a strong vortex on the belly-side of the fuselage formed due to viscous juncture flow interactions between the floor boundary layer and the standoff. This vortex appears to increase in strength with increasing boundary layer thickness. Furthermore the presence of this belly-side vortex led to an increase in the incident angle of attack near the leading edge-strake resulting in onset of dramatic inboard stall.

   3) The observations made using these numerical experiments provide a foundation to explain the similarities seen between the curvilinear and the Cartesian WMLES for in-tunnel configurations even though differences were reported in free-air configuration.

3) **Grid sensitivities and in-tunnel simulations**: The in-tunnel configuration was studied using a sequence of consistently refined grid systems ranging from 100M through 2020M degrees of freedom. Primary grid sensitivity was mainly observed in the pitching moment coefficient for $\alpha > 15^\circ$. Increasing resolution consistently resulted in a more nose-down pitching moment. For $\alpha < 18.9^\circ$, grid levels with 4mm and 3mm resolutions produce essentially identical results. Refinement from 12mm resolution through 4mm resolution resulted in improvement of suction peaks on the outboard portion of the wing, with very little difference observed between 6mm and 4mm grid levels. For $\alpha > 18.9^\circ$ the primary sensitivity to grid resolution switched from outboard wing to the inboard part of the wing between the wing-body juncture and the yehudi break. This sensitivity was due to onset of wing-root separation eventually resulting in a pitch break at $\alpha = 19.9^\circ$ perfectly consistent with observations from the QinetiQ tunnel experiments[34]. Increasing resolution resulted in a larger wing root separation region - causing a larger loss of inboard suction, thus resulting in a more nose-down moment. While some sensitivity between the 4mm and 3mm grids was observed - highlighting the need for additional refinement to establish convergence - it was nonetheless very promising to note the excellent agreement between the previously computed curvilinear WMLES and the experimental oil flow visualizations. The comparisons between curvilinear and Cartesian WMLES appeared to agree quite well at all angles of attack with a slightly higher lift predicted in the Cartesian simulations. Analysis of these discrepancies suggests that differences in the nacelle separation between the two methods and the resulting adjustment of pressure on the main-element directly downstream might partially explain the minor differences in lift. At 15.5° and 17.9° the Cartesian simulations showed a stronger nose-down moment compared to WMLES on the two finest grid levels studied (4mm and 3mm resolution grids). This difference appears to result in higher suction on the outboard flaps in Cartesian grid simulations which

showed better agreement with the experimental data compared to the curvilinear grid simulation. In summary, both curvilinear and Cartesian WMLES predicted consistent and accurate onset of inboard stall mechanism for the in-tunnel configuration with excellent agreement with experiment which was verified by comparing oil flow imagery on the inboard and outboard portions of the wing. This demonstrated objective superiority of WMLES over steady state RANS simulations which predict spurious outboard separation (that becomes increasingly inaccurate with increasing grid resolution) and excess wing-root separation caused by the failure of the RANS closure (as opposed to inadequate convergence as is shown in [38]).

The work presented in this paper constitutes fulfilment of a major CFD Vision 2030 (and NASA Revolutional Computational Aerosciences program) milestone. We demonstrate the potential of WMLES performed using highly efficient and completely automated grid generation as a predictive tool for $C_{L,\max}$ applications. While epistemic uncertainties in regards to appropriate computational modeling of in-tunnel conditions persist, the high solution accuracy seen in the Cartesian Octree formulation shows the massive potential of the method at reducing the solution turn-around times dramatically, by eradicating the need for manual and human-intensive grid generation. We anticipate continued research on both the algorithmic and computational aspects of the method in order to achieve further improvements based on solution accuracy per-unit computational cost metrics.

Acknowledgments

This work was funded by NASA Aeronautics Research Mission Directorate's (ARMD) Transformational Tools and Technologies (T^3) project. Computer time has been provided by the NASA Advanced Supercomputing (NAS) facility at NASA Ames Research Center. Chris Rumsey's (NASA LaRC) inputs on numerical experiments to study floor boundary layer as well as some insight provided by Benedikt Koenig on the existence the floor-standoff juncture vortex were very useful. Jared Duensing (NASA Ames), Leonardo Machado (NASA Ames), Luis Fernandes (NASA Ames) and Elisha Makarevich (formerly NASA Ames, now at Boeing) helped tremendously with overset grid generation for WMLES. Useful feedback on technical content provided by Oliver Browne (NASA Ames) and Jeff Housman (NASA Ames) is also gratefully acknowledged. The authors would also like to thank Man Long Wong (NASA Ames) and Emre Sozer (NASA Ames) for reviewing the paper and providing helpful feedback.

References

[1] Konig, B., Fares, E., Murayama, M., and Ito, Y., "PowerFLOW simulations for the third AIAA high-lift prediction workshop," *2018 AIAA Aerospace Sciences Meeting,* AIAA Paper 2018-1255, 2018. doi:10.2514/6.2018-1255.

[2] Goc, K. A., Lehmkuhl, O., Park, G. I., Bose, S. T., and Moin, P., "Large eddy simulation of aircraft at affordable cost: a milestone in computational fluid dynamics," *Flow*, Vol. 1, 2021.

[3] Kiris, C. C., Ghate, A. S., Duensing, J. C., Browne, O. M., Housman, J. A., Stich, G.-D., Kenway, G., Dos Santos Fernandes, L. M., and Machado, L. M., "High-Lift Common Research Model: RANS, HRLES, and WMLES perspectives for CLmax prediction using LAVA," *AIAA SciTech 2022 Forum,* AIAA Paper 2022-1554, 2022. doi:10.2514/6.2022-1554.

[4] Wang, L., Anderson, W. K., Nielsen, E. J., Balakumar, P., Park, M. A., Carlson, J.-R., Iyer, P. S., and Diskin, B., "Wall-Modeled Large-Eddy Simulations for High-Lift Configurations using FUN3D," *AIAA SCITECH 2022 Forum*, 2022, p. 1555.

[5] Rumsey, C. L., Slotnick, J., Long, M., Stuever, R., and Wayman, T., "Summary of the first AIAA CFD high-lift prediction workshop," *Journal of Aircraft*, Vol. 48, No. 6, 2011, pp. 2068–2079.

[6] Rumsey, C. L., and Slotnick, J. P., "Overview and summary of the second AIAA high-lift prediction workshop," *Journal of Aircraft*, Vol. 52, No. 4, 2015, pp. 1006–1025.

[7] Rumsey, C. L., Slotnick, J. P., and Sclafani, A. J., "Overview and summary of the third AIAA high lift prediction workshop," *Journal of Aircraft*, Vol. 56, No. 2, 2019, pp. 621–644.

[8] Rumsey, C., Slotnick, J., and Woeber, C., "HLPW-4/GMGW-3: Overview and Workshop Summary," AIAA Aviation Paper to appear, 2022.

[9] Slotnick, J. P., Khodadoust, A., Alonso, J., Darmofal, D., Gropp, W., Lurie, E., and Mavriplis, D. J., "CFD vision 2030 study: a path to revolutionary computational aerosciences," Tech. rep., 2014.

[10] Clark, A. M., Slotnick, J. P., Taylor, N. J., and Rumsey, C. L., "Requirements and challenges for CFD validation within the high-lift common research model ecosystem," *AIAA Aviation 2020 Forum,* AIAA Paper 2020-2772, 2020. doi:10.2514/6.2020-2772.

[11] Evans, A., Lacy, D., Smith, I., and Rivers, M., "Test Summary of the NASA Semi-Span High-Lift Common Research Model at the QinetiQ 5-Metre Low-Speed Wind Tunnel," *AIAA Aviation 2020 Forum,* AIAA Paper 2020-2770, 2020. doi:10.2514/6.2020-2770.

[12] Rumsey, C., "4th AIAA High Lift Prediciton Workshop," , 2021. URL https://hiliftpw.larc.nasa.gov/.

[13] Kiris, C. C., Barad, M. F., Housman, J. A., Sozer, E., Brehm, C., and Moini-Yekta, S., "The LAVA computational fluid dynamics solver," *52nd Aerospace Sciences Meeting*, 2014, p. 0070.

[14] Ghate, A. S., Housman, J. A., Stich, G.-D., Kenway, G., and Kiris, C. C., "Scale Resolving Simulations of Corner-Flow Separation in a Wing-Fuselage Juncture," , 2020. URL https://www.nas.nasa.gov/assets/nas/pdf/ams/2020/AMS_20200910_Ghate.pdf, accessed: 2022-04-20.

[15] Ghate, A. S., Housman, J. A., Stich, G.-D., Kenway, G., and Kiris, C. C., "Scale resolving simulations of the NASA Juncture Flow Model using the LAVA solver," *AIAA Aviation 2020 Forum,* AIAA Paper 2020-2735, 2020. doi:10.2514/6.2020-2735.

[16] Stich, G.-D., Housman, J. A., Ghate, A. S., and Kiris, C. C., "Jet noise prediction with large-eddy simulation for chevron nozzle flows," *AIAA Scitech 2021 Forum*, 2021, p. 1185.

[17] Ghate, A. S., Kenway, G. K., Stich, G.-D., Browne, O. M., Housman, J. A., and Kiris, C. C., "Transonic lift and drag predictions using wall-modelled large eddy simulations," *AIAA SciTech 2021 Forum,* AIAA Paper 2021-1439, 2021. doi:10.2514/6.2021-1439.

[18] Stich, G.-D., Ghate, A. S., Housman, J. A., and Kiris, C. C., "Wall Modeled Large Eddy Simulations for NASA's jet noise consensus database of single-stream, round, convergent jets." *AIAA SCITECH 2022 Forum*, 2022, p. 0684.

[19] Ducros, F., Ferrand, V., Nicoud, F., Weber, C., Darracq, D., Gacherieu, C., and Poinsot, T., "Large-eddy simulation of the shock/turbulence interaction," *Journal of Computational Physics*, Vol. 152, No. 2, 1999, pp. 517–549.

[20] Jiang, G.-S., and Shu, C.-W., "Efficient implementation of weighted ENO schemes," *Journal of computational physics*, Vol. 126, No. 1, 1996, pp. 202–228.

[21] Deng, X., and Zhang, H., "Developing high-order weighted compact nonlinear schemes," *Journal of Computational Physics*, Vol. 165, No. 1, 2000, pp. 22–44.

[22] Wong, M. L., and Lele, S. K., "High-order localized dissipation weighted compact nonlinear scheme for shock-and interface-capturing in compressible flows," *Journal of Computational Physics*, Vol. 339, 2017, pp. 179–209.

[23] Nonomura, T., and Fujii, K., "Robust explicit formulation of weighted compact nonlinear scheme," *Computers & Fluids*, Vol. 85, 2013, pp. 8–18.

[24] Tseng, Y.-H., and Ferziger, J. H., "A ghost-cell immersed boundary method for flow in complex geometry," *Journal of computational physics*, Vol. 192, No. 2, 2003, pp. 593–623.

[25] Seifert, A., and Pack, L. G., "Active flow separation control on wall-mounted hump at high Reynolds numbers," *AIAA journal*, Vol. 40, No. 7, 2002, pp. 1363–1372.

[26] Kiris, C. C., Stich, D., Housman, J. A., Kocheemoolayil, J. G., Barad, M. F., and Cadieux, F., "Application of Lattice Boltzmann and Navier-Stokes methods to NASA's wall mounted hump," *2018 Fluid Dynamics Conference*, 2018, p. 3855.

[27] Addy, H. E., *Ice accretions and icing effects for modern airfoils*, National Aeronautics Administration, Glenn Research Center, 2000.

[28] Manoha, E., Bulté, J., and Caruelle, B., "LAGOON: an experimental database for the validation of CFD/CAA methods for landing gear noise prediction," *14th AIAA/CEAS aeroacoustics conference (29th AIAA aeroacoustics conference)*, 2008, p. 2816.

[29] Wong, M. L., Kenway, G. K., Ghate, A. S., Stich, G.-D., and Kiris, C. C., "Predictions of LAGOON Nose Landing Gear Flow and Noise using Wall-Modeled Large-Eddy Simulations," *28th AIAA/CEAS Aeroacoustics Conference*, 2022.

[30] Vreman, A., "An eddy-viscosity subgrid-scale model for turbulent shear flow: Algebraic theory and applications," *Physics of Fluids*, Vol. 16, No. 10, 2004, pp. 3670–3681.

[31] Gottlieb, S., Shu, C.-W., and Tadmor, E., "Strong stability-preserving high-order time discretization methods," *SIAM review*, Vol. 43, No. 1, 2001, pp. 89–112.

[32] Rumsey, C., "QinetiQ 5m Wind Tunnel Modeling," , 2022. URL https://hiliftpw.larc.nasa.gov/Workshop4/Geometry/Q5m_Tunnel_Modeling_V01.pdf, accessed: 2022-04-28.

[33] Konig, B., Singh, D., Fares, E., and Wright, M., "Transonic Lattice Boltzmann Simulations of the NASA-CRM in the European Transonic Windtunnel," *2018 Applied Aerodynamics Conference*, 2018, p. 3171.

[34] Lacy, D. S., and Clark, A. M., "Definition of Initial Landing and Takeoff Reference Configurations for the High Lift Common Research Model (CRM-HL)," *AIAA Aviation 2020 Forum,* AIAA Paper 2020-2771, 2020. doi:10.2514/6.2020-2771.

[35] Kiris, C., Ghate, A., Browne, O., Slotnick, J., and Larsson, J., "HLPW-4/GMGW-3: Wall-Modeled LES and Lattice-Boltzmann Technology Focus Group Workshop Summary," AIAA Aviation Paper to appear, 2022.

[36] Koklu, M., Lin, J. C., Hannon, J. A., Melton, L. P., Andino, M. Y., Paschal, K. B., and Vatsa, V. N., "Investigation of the Nacelle/Pylon Vortex System on the High-Lift Common Research Model," *AIAA Journal*, Vol. 59, No. 9, 2021, pp. 3748–3763.

[37] Duensing, J. C., Housman, J. A., Fernandes, L. S., Machado, L. G., and Kiris, C. C., "A Reynolds-Averaged Navier-Stokes Perspective for the High Lift Common Research Model Using LAVA," *AIAA Aviation Paper to appear*, 2022.

[38] Browne, O., Housman, J., Kenway, G., Ghate, A., and Kiris, C., "A Hybrid RANS-LES Perspective for the High Lift Common Research Model Using LAVA," *AIAA Aviation 2022 Forum*, 2022.

[39] Garner, H. C., Rogers, E., Acum, W., and Maskell, E., "Subsonic wind tunnel wall corrections," Tech. rep., ADVISORY GROUP FOR AEROSPACE RESEARCH AND DEVELOPMENT NEUILLY-SUR-SEINE (FRANCE), 1966.

[40] Murayama, M., Yokokawa, Y., Tanaka, K., Yamamoto, K., and Ito, T., "Numerical simulation of half-span aircraft model with high-lift devices in wind tunnel," *46th AIAA Aerospace Sciences Meeting and Exhibit,* AIAA Paper 2008-333, 2008. doi:10.2514/6.2008-333.

[41] Yokokawa, Y., Murayama, M., Uchida, H., Tanaka, K., Ito, T., Yamamoto, K., and Yamamoto, K., "Aerodynamic influence of a half-span model installation for high-lift configuration experiment," *48th AIAA Aerospace Sciences Meeting Including the New Horizons Forum and Aerospace Exposition,* AIAA Paper 2010-684, 2010. doi:10.2514/6.2010-684.

[42] Singh, D., Konig, B., Fares, E., Murayama, M., Ito, Y., Yokokawa, Y., and Yamamoto, K., "Lattice-Boltzmann simulations of the JAXA JSM high-lift configuration in a wind tunnel," *AIAA Scitech 2019 Forum*, 2019, p. 1333.

[43] Giguere, P., and Selig, M., "Study of semi-span model testing techniques," *14th Applied Aerodynamics Conference,* AIAA Paper 1996-2388, 1996. doi:10.2514/6.1996-2388.

[44] Rogers, S., Roth, K., and Nash, S., "CFD validation of high-lift flows with significant wind-tunnel effects," *18th Applied Aerodynamics Conference*, 2000, p. 4218.